ARTICLE IN PRESS

ISA Transactions xxx (xxxx) xxx

Contents lists available at ScienceDirect

ISA Transactions

journal homepage: www.elsevier.com/locate/isatrans

Research Article

Cooperative control for a ROV-based deep-sea mining vehicle with learned uncertain nonlinear dynamics

Yuheng Chen [a], Haicheng Zhang [a,b,*], Weisheng Zou [a], Haihua Zhang [c], Daolin Xu [a]

[a] College of Mechanical and Vehicle Engineering, Hunan University, Changsha, Hunan 410082, China
[b] Greater Bay Area Institute for Innovation, Hunan University, Guangzhou 511300, China
[c] Taihu Laboratory of Deepsea Technological Science Lian Yun Gang Center, Jiangsu 222005, China

ARTICLE INFO

Keywords:
Deep-sea mining
Dynamic modeling
Model predictive control
ROV
Path tracking

ABSTRACT

To overcome the bottleneck problem of the track slippage of the tracked mining vehicle in the traditional deep-sea mining system, this paper proposes an enhanced remotely-operated vehicle (ROV)-based deep-sea mining system. A ROV-based Deep-sea Mining Vehicle (RDMV), consisting of two ROVs and a mining robot (MRT), is instead of the traditional tracked Deep-sea mining vehicle. Firstly, the dynamic model of the RDMV as a control object is established based on Lagrangian function. Secondly, a cooperative control strategy is proposed for traction and sinking control of the RDMV. A distributed model predictive control (DMPC)-based controller is developed to obtain virtual speed control laws to meet the control objects. To track the virtual speed control laws, a learning-based model predictive control (LMPC)-based controller is investigated to compute the ROVs' optimal control input, where a Kinky Inference (KI) prediction function is introduced in the state transition model to estimate the unknown external disturbances under random noise. Finally, the feasibility and the superiority of the LMPC controller is preliminarily verified in a degenerate individual motion control of a ROV, and then the cooperative control strategy is proven to be effective through numerical simulations.

1. Introduction

To alleviate the shortage of mineral resources on land, exploitation of deep-sea mineral resources from the thousands of meters of ocean floor, has been on the agenda since 1960s [1]. Deep-sea mining system is the key equipment for commercial exploitation. However, deep-sea mining is still in a research and exploration stage for the main reason that deep-sea mining systems have not yet reached the standards for commercial exploitation.

At present, a hydraulic lift deep-sea mining system, where a deep-sea tracked mining vehicle tracks the mining path to collect the mineral resources, is considered as a commercially viable option [2,3]. However, the contradiction of large grip and large subsidence on the seafloor sediments becomes the inherent shortcoming of the traditional heavy tracked mining vehicle [4]. To overcome the inherent shortcoming, a novel ROV-based deep-sea mining system is firstly proposed [5,6]. A ROV-based deep-sea mining vehicle (RDMV), consisting of a towing remotely-operated vehicle (TROV) and a mining robot (MRT), is instead of the tracked mining vehicle. The TROV tows the MRT to slide orderly on the seabed through an articulated steel frame, and the MRT's body sinking can be controlled by adjusting vertical component of the internal force in the articulated rigid frame. However, the TROV faces a contradiction between providing efficient traction for the MRT and maintaining effective control over the MRT's body sinking [6]. To further improve the ROV-based mining system, a hanging remotely-operated vehicle (HROV) is introduced, as shown in Fig. 1. The TROV now just plays the role of the MRT's motion control in the horizontal plane, and the HROV keeps the synchronization with the MRT to provide vertical tensile force via the two-force member.

The cooperative control strategy for the TROV and the HROV is the key issue, and research on cooperative control strategy for a multiple-ROV system is a hot topic [7,8]. The control objective is to maintain all the ROVs in a fixed or a time-varying formation, and distributed model predictive control (DMPC) is an effective control method for the cooperative control of a multiple-ROV system [9]. It can separately construct the optimal control problem (OCP) to handle the constraints and multiple optimization variables, and the control objective is transformed into the motion control of individual ROVs in the multiple-ROV

* Correspondence to: College of Mechanical and Vehicle Engineering, Hunan University, Changsha 410082, PR China.
E-mail addresses: chenyuheng@hnu.edu.cn (Y. Chen), zhanghc@hnu.edu.cn (H. Zhang), zouweisheng@sina.com (W. Zou), zhanghaihua@702sh.com (H. Zhang), dlxu@hnu.edu.cn (D. Xu).

https://doi.org/10.1016/j.isatra.2025.02.033
Received 6 June 2024; Received in revised form 27 February 2025; Accepted 27 February 2025
Available online 1 March 2025

Please cite this article as: Yuheng Chen et al., *ISA Transactions,* https://doi.org/10.1016/j.isatra.2025.02.033

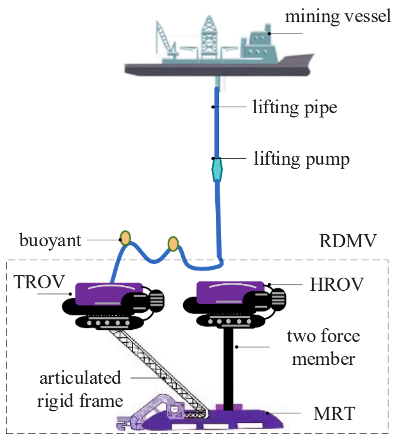

Fig. 1. ROV-based deep-sea mining system.

system.

Model predictive control (MPC) can formulate a constrained optimal control problem to achieve control objectives of a nonlinear system [10–13]. However, control performance depends on an accurate control-oriented model of the underlying system. For motion control of an individual ROV using MPC control method, the model mismatch, which consists of the unknown external current disturbances, parametric uncertainties of the control system, is the key issue to degrade the control performance [14]. To address the model mismatch, one effective strategy is to introduce a disturbance observer [15]. Chengqi Longet et al. introduce a EKF-based disturbance observer to accurately estimate ocean current disturbance, which increases the extra dimension of the control model to formulate an optimal control problem [16]. The extra dimension will bring great computational burden when solving the optimal control problem, and the control performance is enhanced at the expense of real-time performance. Learning-based model predictive control (LMPC) is another effective strategy, where the complex nonlinear dynamics function can be accurately estimated using a data-driven method, and is further utilized as the state transition model to formulate an optimal control problem [17,18]. One approach is to fit the nonlinear dynamics function via neural network [19,20]. The Koopman operator, stemming from linearization techniques, acts as a crucial intermediary linking the system state to the nonlinear dynamics function. Harnessing the koopman operator as prior knowledge has showcased the proficient learning performance of hierarchical neural networks [21]. As such, the control performance of the LMPC relies heavily on the pre-trained the neural network it employs. However, extensive and sufficient training data of the complex system is hard to be obtained. Another approach is to formulate a map between the state and the nonlinear function using Kinky Inference (KI) prediction [22,23]. This approach could perform inference over the nonlinear function values without the need for pre-training like in neural networks. Combining distributionally robust optimization and stochastic model predictive, a training set that matches the true disturbance distribution to some extent is a priori knowledge, and then the map between the state and disturbance distribution is formulated [23]. Kaikai Zheng introduces a nonparametric learning (NPL) method to develop the search-based-map via KI prediction function, where a data selection mechanism is proposed to address the issue of real-time performance impacted by an excessive number of sampling points in the dataset [18]. However, the data selection mechanism fails to remove redundant sampling points. As real-time nonlinear function values are highly correlated with the most recent sampling points, older sampling points may gradually lose relevance.

How to analyze the complex dynamics of the RDMV to establish its dynamic model is another issue. Hydrodynamic force of the TROV and HROV can represents as empirical formula [16]. Based on the interaction force of the track and the seabed sediment [25], that of the MRT and the seabed sediment can be easily further deduced. However, the position constraint introduced articulated steel frame and the two-force moment makes it difficult to establish the mechanical model of TROV, HROV and MRT. To overcome the issues, the dynamic model of the RDMV and its cooperative control strategy for tracking and sinking control of the RDMV is investigated in this paper, and the main contributions are as follows:

1. An enhanced ROV-based deep-sea mining system is proposed, and a three-dimensional dynamic model of the RDMV is established based on Lagrangian function for further numerical simulation analysis.
2. An enhanced NPL method is developed based on the Lazily Adapted Constant Kinky Inference (LACKI) scheme to formulate a search-based map between the sampled dataset and the RDMV's complex nonlinear dynamics function [24]. Compared with the existing method [18], a learning rule to formulate the sampled dataset is introduced to enhance its real-time performance. The method maintains a sufficiently small number of samples to reduce the computational complexity of the KI prediction function, and its estimation deviation is rigorously proven to be bounded.
3. A hierarchical cooperative control strategy consists of a DMPC controller and a LMPC controller is investigated. The DMPC controller is designed based on the RDMV's kinematic model to obtain a virtual speed control law, which meets the cooperative control object. The learned RDMV's complex nonlinear dynamics function by the enhanced NPL method is utilized to address the model mismatch, and then the LMPC controller is designed to track the virtual speed control law.

The remainder of this paper is organized as follows. Section 2 introduces the dynamic model of the RDMV. Section 3 introduces the novel nonparameteric learning method. Section 4 proposes the cooperative control strategy. Section 5 gives the results and discussion.

2. Dynamic model of the RDMV

In this section, the dynamic model of the RDMV is derived as the control objection in numerical simulation. Compared to the towing force, the connecting force of the flexible pipe acting on the TROV can be neglected due to the saddle shape of the compensation soft pipe. Additionally, the mass of steel frame and the two-force member is all small, compared with the mass of the TROV, HROV and MRT. To simplify the dynamic model, the forces from the flexible pipe, as well as the mass of the steel frame and the two-force member are ignored. Further simplifications are also made during the preliminary research of the dynamic model.

1. Suppose the MRT and the steel frame are solid, while the TROV is modeled as articulated. Drawing inspiration from the bicycle model in an Ackermann steering vehicle [26], the TROV functions as a steering mechanism, with the TROV and MRT analogous to the front wheel and the rear wheel, respectively. To ensure stable steering, the steering angle of the TROV and its angular velocity around the steel frame are kept small. This leads to the small angle assumption in the subsequent dynamic modeling.
2. Suppose the TROV and HROV maintain stability during roll and pitch motions, enabling the roll angle and pitch angle to quickly and smoothly to their initial states after momentary disturbances [14]. Consequently, degrees of freedom (DOFs) of pitching and rolling can be neglected.
3. Suppose the TROV tows the MRT at a constant depth, with MRT sliding on the seafloor surface, and their dynamics are considered only in the horizontal plane. The kinematic relationship between the DOFs of the TROV and the MRT is analyzed firstly. Subsequently, it is sufficient to focus on the three DOFs dynamics of the TROV.

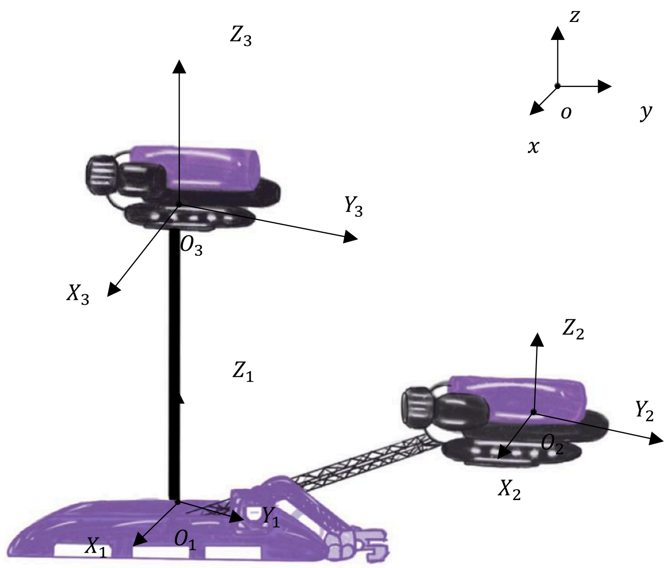

Fig. 2. Coordinate frame of the RDMV.

4. Suppose the MRT and the two-force member, as well as the HROV and the two-force member, are articulated. The coordinates of the HROV can be derived from the attitude angle of the two-force member. Therefore, it is necessary to analyze the dynamics of the two-force member's attitude angle, treating the yaw motion of the HROV separately.

2.1. Kinematic model

Firstly, the global coordinate frame and the local coordinate frame of the TROV, HROV and MRT are defined, as illustrated in Fig. 2. $O-xyz$ denotes the global coordinate system. $O_1-X_1Y_1Z_1$ denotes the MRT's local coordinate system, $O_2-X_2Y_2Z_2$ denotes the TROV's local coordinate system, and $O_3-X_3Y_3Z_3$ denotes the HROV's local coordinate system. Denote the surge speeds of the MRT and the TROV by u_1 and u_2, and their sway speeds are denoted by v_1 and v_2. From Fig. 2, the transformation relationship of the surge and sway speeds is given:

$$u_1 = u_2\cos\delta - v_2\sin\delta, v_1 = v_2\cos\delta + u_2\sin\delta \tag{1}$$

where δ is the horizontal rotation angle of the TROV around the steel frame.

Denote the rotation angle of the two-force member around the x and y axes by φ and θ, where $p := \dot{\varphi}$ and $q := \dot{\theta}$ are the angular speeds. The transformation relationship of the global coordinates of the HROV and the MRT is established:

$$\begin{aligned} x_3 &= x_1 + L_1\cos\varphi\sin\theta, \\ y_3 &= y_1 + L_1\sin\varphi, \\ \dot{z} &= w, \\ dz &= L_1\cos\theta\cos\varphi + h - z \end{aligned} \tag{2}$$

where L_1 is the length of the two-force member. h is the MRT's height. Denote the MRT's body sinkage by d_z. x_1 and y_1 are the global coordinates of MRT. The global coordinates of the HROV are denoted by x_3, y_3 and z. Let w denote the heave speed.

Based on the rigid body kinematics, the surge and the sway speeds of the HROV can be calculated:

$$\begin{bmatrix} u_3 \\ v_3 \end{bmatrix} = J_3\left(J_1\begin{bmatrix} u_1 \\ v_1 \end{bmatrix} + T_m\right) \tag{3}$$

where J_1 is the transformation matrix from $O_1-X_1Y_1Z_1$ to $O-xyz$. J_3 is the transformation matrix from $O-xyz$ to $O_3-X_3Y_3Z_3$. Matrix T_m represents the transport motion:

$$\begin{aligned} J_3 &= \begin{bmatrix} \cos\psi_3 & \sin\psi_3 \\ -\sin\psi_3 & \cos\psi_3 \end{bmatrix}, \\ J_1 &= \begin{bmatrix} \cos\psi_1 & -\sin\psi_1 \\ \sin\psi_1 & \cos\psi_1 \end{bmatrix}, \\ T_m &= \begin{bmatrix} qL_{1z} \\ -pL_{1z} \end{bmatrix}, \\ \psi_3 &= \omega_3 \end{aligned}$$

where $L_{1z} = L_1\cos\theta\cos\varphi$ denotes the projected length of the two-force member on the z axis. Denote the HROV's yaw angle and yaw rate by ψ_3 and ω_3.

According to bicycle model [26], MRT's yaw rate ω_1 is related to the surge speed of the MRT u_1 and the horizontal rotation angleof the ROV around the steel frame δ:

$$\dot{\psi}_1 = \omega_1 = \frac{u_1\delta}{L_2}, \dot{\delta} = \omega_2 \tag{4}$$

where ψ_1 is MRT's yaw angle. L_2 denotes the horizontal projection length of the steel frame. ω_2 is TROV's yaw rate.

2.2. Kinetic model

The kinetic equation of the TROV with 3 DOFs will be deduced using Lagrangian method. Firstly, the Lagrange function, consisting of the kinetic energy of the TROV K_2 and the kinetic energy of the MRT K_1, is expressed as:

$$\begin{aligned} L_g(q,\dot{q}) &= K_1 + K_2 - E \\ K_1 &= \frac{1}{2}m_1\left(u_1^2 + v_1^2\right) + \frac{1}{2}I_1\omega_1^2 = \frac{1}{2}m_1\left(u_1^2 + v_1^2\right) + \frac{1}{2}I_1\left(\frac{u_1\delta}{L_2}\right)^2 \\ K_2 &= \frac{1}{2}m_2\left(u_2^2 + v_2^2\right) + \frac{1}{2}I_2\omega_2^2 \end{aligned} \tag{5}$$

where I_1 and I_2 denote the rotational inertia of the MRT and the TROV, respectively. The masses of the MRT and the TROV are represented by m_1 and m_2, respectively. The state and its first order derivative are defined by $q = (x_2, y_2, \delta)^{\mathrm{T}}$ and $\dot{q} = (u_2, v_2, \omega_2)^{\mathrm{T}}$. Since the 3 DOFs are considered in the horizontal plane, the potential energy of E is treated as a constant.

Finally, the Lagrangian equation is expressed as:

$$\frac{d}{dt}\frac{L_g}{\partial\dot{q}} - \frac{L_g}{\partial q} = F_{TROV} + \mathscr{J}(F_{MRT} + F_{link2}) + \tau_2 + \tau_{e2} + \tau_{\omega 2} \tag{6}$$

where F_{TROV} is the generalized hydrodynamic force of the TROV in local coordinate system $O_2 - X_2Y_2$. Denote the generalized interaction force between the MRT and seafloor sediments in local coordinate system $O_2-X_2Y_2$ by F_{MRT}. The control input of the TROV is denoted by $\tau_2 = (F_{X2}, F_{Y2}, T_{N2})^{\mathrm{T}}$, and $\tau_e \in \mathscr{R}^{3\times 1}$ represents the unmodeled bounded external ocean current disturbance and model mismatch from parametric uncertainty. Additionally, the random bounded process noise force from the rugged seafloor sediments is denoted by $\tau_{\omega 2} \in \mathscr{R}^{3\times 1}$ [27]. Denote internal force of the two-force member and its projection in the MRT's local coordinate frame by T_{link} and F_{link2}. $\mathscr{J}_1$ is the transformation matrix from $O_1-X_1Y_1Z_1$ to $O_2-X_2Y_2Z_2$.

$$F_{link2} = \begin{bmatrix} \cos\phi\sin\theta\cos\psi_1 T_{link} + \sin\phi\sin\psi_1 T_{link} \\ \sin\phi\cos\psi_1 T_{link} - \cos\phi\sin\theta\sin\psi_1 T_{link} \\ 0 \end{bmatrix},$$

$$\mathscr{J}_1 = \begin{bmatrix} \cos\delta & \sin\delta & 0 \\ -\sin\delta & \cos\delta & 0 \\ 0 & 0 & 0 \end{bmatrix}$$

Substitute Eq. 5 into Eq. 6, and the left side of Eq. 6 becomes:

$$\frac{d}{dt}\frac{L_g}{\partial u_2} - \frac{L_g}{\partial x_2} = (m_1 + m_2)\dot{u}_2 + \frac{I_1\delta^2}{L_2^2}\dot{u}_2 = (m_1 + m_2 + m_\delta)\dot{u}_2 \tag{7}$$

$$\frac{d}{dt}\frac{L_g}{\partial v_2} - \frac{L_g}{\partial y_2} = (m_1 + m_2)\dot{v}_2 \tag{8}$$

$$\frac{d}{dt}\frac{L_g}{\partial \omega_2} - \frac{L_g}{\partial \delta} = I_2\dot{\omega}_2 - \frac{I_1 u_2^2}{L_2^2}\delta \tag{9}$$

where $m_\delta = I_1\delta^2/L^2$ denotes the added mass of the MRT in the horizontal rotation angle DOF.

Based on the previous research [16], an empirical formula can be employed to express the generalized hydrodynamic force of the ROV F_{ROV}. This force encompasses the add mass force, centripetal and Coriolis force and hydrodynamic damping force:

$$F_{TROV} = M_{A2}\dot{q} + (C_2 \quad + D_2)q \tag{10}$$

where the add mass matrix of the TROV is denoted by $M_{A2} = \mathrm{diag}(X_{\dot{u}}, Y_{\dot{v}}, N_{\dot{r}})$, with $X_{\dot{u}}, Y_{\dot{v}}$ and $N_{\dot{r}}$ representing the hydrodynamic coefficients. Denote the hydrodynamic damping matrix of the TROV by $D_2 = \mathrm{diag}(X_u + X_{uu}|u_2|, Y_v + Y_{vv}|v_2|, N_r + N_{rr}|\omega_2|)$, where the symbols X_u, X_{uu}, Y_v, Y_{vv}, N_r and N_{rr} are hydrodynamic damping coefficients. Centripetal and Coriolis force matrix of the TROV C_2 can be expressed as:

$$C_2 = \begin{bmatrix} 0 & 0 & (X_{vr} + m_2)v_2 + X_{rr}\omega_2 \\ 0 & Y_{uv}u_2 & (Y_{ur} - m_2)u_2 \\ -m_2v_2 & (N_{uv} + m_2)u_2 & N_{ur}u_2 \end{bmatrix} \tag{11}$$

where X_{vr}, X_{rr}, Y_{uv}, Y_{ur}, N_{uv} and N_{ur} are hydrodynamic coefficients.

To further establish Lagrangian Eq. (7), the interaction force F_{MRT} need be deduced. Since the soft seafloor sediment can be considered as plastic soil [28], the MRT is subjected to longitudinal resistance F_R and lateral friction force f due to a triangular load. Considering plastic soil, a lateral friction coefficient relative to the turning radius is employed to express the lateral friction force [29]:

$$f = \mu_y\frac{F_N}{2} = \mu_y\frac{W - T_{link}\cos\phi\cos\theta}{2} \tag{12}$$

where W represents the underwater weight of the MRT. Denote the support force of the MRT by F_N, and μ_y is the lateral friction coefficient:

$$\mu_y = E_1\left(1 - e^{\frac{C_I blE_2}{m_1}}\right)\left(1 - e^{\frac{C_I blE_3 r}{m_1}}\right) \tag{13}$$

in which l and b represent the length and width of the MRT. C_I represents the terrain cone index. Denote the turning radius of the MRT by r. E_1, E_2 and E_3 are empirical coefficients.

The lateral friction force f can be equivalent to the TROV's turning resistance moment M_{o_2} with respect to O_2 [30]:

$$M_{o_2} = \left(\frac{3}{4}l + L\right)f - \left(\frac{1}{4}l + L\right)f = \frac{1}{2}lf = \frac{\mu_y Wl}{4} \tag{14}$$

Then, the generalized interaction force F_M can be obtained:

$$F_{MRT} = (-F_R\cos\delta, F_R\sin\delta, -\mathrm{sg}(\omega_1)M_{o_2}) \tag{15}$$

where $\mathrm{sg}(\bullet)$ is a function denoted as $\mathrm{sg}(x) = 1, x > 0; \mathrm{sg}(x) = -1, x < 0; \mathrm{sg}(x) = 0, x = 0$.

Due to the sinkage on the soft seafloor sediment [25,30], the longitudinal resistance F_R consists of a compaction resistance F_{Rc} and a bulldozing resistance F_{Rb}:

$$F_R = F_{Rc} + F_{Rb} \tag{16}$$

where the underwater weight of the MRT and the soil properties will influence the sinkage characteristics [31].

Based on Bekker's pressure–sinkage relationship [32], the compaction resistance F_{Rc} can be expressed as follows:

$$F_{Rc} = \frac{b}{2f}\Delta z^2 - \frac{be}{\tilde{f}}\Delta z \tag{17}$$

where $p = (W - T_{link}\cos\phi\cos\theta)/bl$ is the normal pressure from the MRT acting on the soil. e and $\tilde{f}$ satisfy the empirical formula [33]:

$$\tilde{f} = 1.99 - 0.112\tau \tag{18}$$

$$\begin{gathered} e = 6.725 - 2.568\tau + 0.245\tau^2, \tau \geq 5\text{kPa} \\ e = 0, \tau < 5\text{kPa} \end{gathered} \tag{19}$$

in which τ is the shear strength of soft seafloor sediment:

$$\tau = c + p\tan\Phi \tag{20}$$

where c is the apparent cohesion, and Φ is the angle of internal shearing resistance.

Meanwhile, the bulldozing force can be expressed as a function of the mechanical properties of the soft seafloor sediment and the sinkage [32, 34]:

$$F_{Rb} = \left(\frac{1}{2}r_s\Delta z^2 k_{pr} + c\Delta z k_{pc}\right)b \tag{21}$$

where r_s is the density of the sediment. k_{pr} and k_{pc} denote the coefficients of passive earth pressure:

$$k_{pr} = \left(\frac{2N_r}{\tan\Phi} + 1\right)\cos^2\Phi, k_{pc} = (N_c - \tan\Phi)\cos^2\Phi \tag{22}$$

Denote the speed vector of the HROV by $\nu = (u_3, v_3, w, \omega_3)^{\mathrm{T}}$. The dynamics equation of the HROV can also be established from an empirical formula:

$$(M_3 + M_{A3})\dot{\nu} = (C_3 + D_3)\nu + F_{link3} + \tau_3 + \tau_{e3} \tag{23}$$

where the add mass matrix of the HROV is denoted by $M_{A3} = \mathrm{diag}(X'_{\dot{u}}, Y'_{\dot{v}}, Z_{\dot{w}}, N'_{\dot{r}})$, with $X'_{\dot{u}}, Y'_{\dot{v}}$, $Z_w$and $N'_{\dot{r}}$ representing the hydrodynamic coefficients. $M_3 = \mathrm{diag}(m_3, m_3, m_3, I_3)$ is the inertial mass matrix of the HROV. The control input of the HROV is denoted by $\tau_3 = (F_{X3}, \quad F_{Y3}, \quad F_Z, T_{N3})^{\mathrm{T}}$, and $\tau_e \in \mathscr{R}^{4\times1}$ also represents the unmodeled bounded external ocean current disturbance and the model mismatch arising from parametric uncertainty. Denote the hydrodynamic damping matrix of the HROV by $D_3 = \mathrm{diag}(X'_u + X'_{uu}|u_3|, Y'_v + Y'_{vv}|v_3|, Z_w + Z_{ww}|w|, N'_r + N'_{rr}|\omega_3|)$, where the symbols X'_u, X'_{uu}, Y'_v, Y'_{vv}, N'_r, Z_w, Z_{ww}, and N'_{rr} are hydrodynamic damping coefficients. Centripetal and Coriolis force matrix of the HROV is denoted by C_3. F_{link3} represents the projection of the internal force of the two-force member in the HROV's local coordinate system.

$$C_3 = \begin{bmatrix} 0 & 0 & 0 & (X'_{vr}+m_3)v_3 + X'_{rr}\omega_3 \\ 0 & Y'_{uv}u_3 & 0 & (Y'_{ur}-m_3)u_3 \\ 0 & 0 & Z_{uw}u_3 & 0 \\ -m_3v_3 & (N'_{uv}+m_3)u_3 & 0 & N'_{ur}u_3 \end{bmatrix}$$

$$F_{link3} = \begin{bmatrix} -\cos\phi\sin\theta\cos\psi_3 T_{link} - \sin\phi\sin\psi_3 T_{link} \\ -\sin\phi\cos\psi_3 T_{link} + \cos\phi\sin\theta\sin\psi_3 T_{link} \\ -T_{link}\cos\phi\cos\theta \\ 0 \end{bmatrix}$$

where X'_{vr}, X'_{rr}, Y'_{uv}, Y_{ur}, N'_{uv}, Z_{uw} and N'_{ur} are hydrodynamic coefficients.

Based on the rigid body kinematics, the rotation angle acceleration of the two-force member can be calculated based on the relative linear acceleration of the HROV and the MRT in the global coordinate frame:

$$\begin{bmatrix} \dot{p} \\ \dot{q} \end{bmatrix} = \begin{bmatrix} -(a_{y3}-a_{y1})/L_{1z} \\ (a_{x3}-a_{x1}) \quad /L_{1z} \end{bmatrix} \tag{24}$$

where a_{x1} and a_{y1} represent the linear acceleration of MRT in the global coordinate frame. a_{x3} and a_{y3} represent the linear acceleration of HROV in the global coordinate frame:

$$\begin{bmatrix} a_{x1} \\ a_{y1} \end{bmatrix} = J_1\begin{bmatrix} \dot{u}_1 \\ \dot{v}_1 \end{bmatrix}, \begin{bmatrix} a_{x3} \\ a_{y3} \end{bmatrix} = J_3^{-1}\begin{bmatrix} \dot{u}_3 \\ \dot{v}_3 \end{bmatrix} \tag{25}$$

Based on transformation relationship (1), the acceleration of the MRT's surge and sway speeds is calculated as:

$$\begin{aligned} \dot{u}_1 &= \dot{u}_2\cos\delta - \dot{v}_2\sin\delta - \dot{\delta}(u_2\sin\delta + v_2\cos\delta) \\ \dot{v}_1 &= \dot{v}_2\cos\delta + \dot{u}_2\sin\delta + \dot{\delta}(u_2\cos\delta - v_2\sin\delta) \end{aligned} \tag{26}$$

Based on the derivation of kinetic Model of the RDMV, the discretized state space of the TROV and the HROV, which satisfies Lipschitz nonlinear model, can be obtained [35]:

$$\begin{aligned} \mathscr{X}_2(k+1) &= \mathscr{A}_2\mathscr{X}_2(k) + \mathscr{B}_2U_2(k) + f^2(\mathscr{X}_2(k)) + \omega_2(k) \\ \mathscr{X}_3(k+1) &= \mathscr{A}_3\mathscr{X}_3(k) + \mathscr{B}_3U_3(k) + f^3(\mathscr{X}_3(k)) + \omega_3(k) \end{aligned} \tag{27}$$

where $\omega_2 \in \mathscr{R}^{4\times1}$ is the unknown bounded process noise from the rugged seafloor transmitted by the steel frame. $\omega_3 \in \mathscr{R}^{5\times1}$ also represents unknown bounded process noise from the rugged seafloor, transmitted by the two-force member. The state of the TROV is denoted by $\mathscr{X}_2 := (u_2, v_2, \omega_2, \delta)^{\mathrm{T}}$, and the state of the HROV is denoted by $\mathscr{X}_3 := (u_3, v_3, \omega_3, w, z)^{\mathrm{T}}$. The control inputs satisfy $U_2 := \tau_2$, $U_3 := \tau_3$. The state matrices $\mathscr{A}_2$ and $\mathscr{A}_3$, as well as the control matrices $\mathscr{B}_2$ and $\mathscr{B}_3$ are given as:

$$\mathscr{A}_2 = \mathscr{M}_2^{-1}\begin{bmatrix} 1+T_RX_u & 0 & 0 & 0 \\ 0 & 1+T_RY_v & 0 & 0 \\ 0 & 0 & 1+T_RN_r & 0 \\ 0 & 0 & T_R & 1 \end{bmatrix}, \mathscr{B}_2 = \mathscr{M}_2^{-1}\begin{bmatrix} T_R & 0 & 0 \\ 0 & T_R & 0 \\ 0 & 0 & T_R \\ 0 & 0 & 0 \end{bmatrix},$$
$$\mathscr{M}_2 = \mathrm{diag}(m_1+m_2+m_\delta - X_{\dot{u}}, m_1+m_2-Y_{\dot{v}}, I_2 - N_{\dot{r}}, 1) \tag{28}$$

$$\mathscr{A}_3 = \begin{bmatrix} \mathscr{M}_3^{-1} & 0_{4\times1} \\ 0_{1\times4} & 1 \end{bmatrix}\begin{bmatrix} 1+T_RX'_u & 0 & 0 & 0 & 0 \\ 0 & 1+T_RY'_v & 0 & 0 & 0 \\ 0 & 0 & 1+T_RN'_r & 0 & 0 \\ 0 & 0 & 0 & 1+T_RZ'_w & 0 \\ 0 & 0 & 0 & T_R & 1 \end{bmatrix},$$
$$\mathscr{B}_3 = \begin{bmatrix} \mathscr{M}_3^{-1} \\ 0_{1\times4} \end{bmatrix}\begin{bmatrix} T_R & 0 & 0 & 0 \\ 0 & T_R & 0 & 0 \\ 0 & 0 & T_R & 0 \\ 0 & 0 & 0 & T_R \\ 0 & 0 & 0 & 0 \end{bmatrix}, \mathscr{M}_3 = \mathrm{diag}(m_3 - X'_{\dot{u}}, m_3 - Y'_{\dot{v}}, I_3 - N'_{\dot{r}}, m_3 - Z_{\dot{w}}) \tag{29}$$

where T_R is the sampling time of the LMPC controller. The mass matrices are denoted by $\mathscr{M}_2$ and $\mathscr{M}_3$. Note that the added mass m_δ is related to the horizontal rotation angle δ, and the state matrix $\mathscr{A}_2$ and the control matrix $\mathscr{B}_2$ are time-varying. To align with the Lipschitz nonlinear model [35], the added mass m_δ is simplified as a constant.

Indeed, the construction of a real system can provide the rigorous validation for the deduced dynamic model. Due to the limited funding and space for testing large-scale system, a discussion on the rationality of the modeling process is given. The RDMV consists of two ROVs and a MRT, and the kinetic model of the ROV is a classic model summarized from existing literature [36]. Besides, the interaction force of the MRT is also deduced from the above literatures. Finally, the kinetic model of the RDMV is obtained using classic Lagrangian and Newtonian methods.

The dynamic parameters are difficult to obtain accurately, and an uncertain term representing the model mismatch due to parametric uncertainty is introduced. Then, the function $f_2(\mathscr{X}_2)$, consisting of the nonlinear dynamics function of the MRT and the TROV, $g_2(\mathscr{X}_2)$, the model mismatch, $\tilde{g}_2$ and the unknown external ocean current disturbance, h_{e2}, is given as:

$$f_2(\mathscr{X}_2) = \begin{bmatrix} \mathscr{M}_2^{-1} \\ 0_{1\times4} \end{bmatrix}\left(g_2(\mathscr{X}_2) + \tilde{g}_2\right) + h_{e2} \tag{30}$$

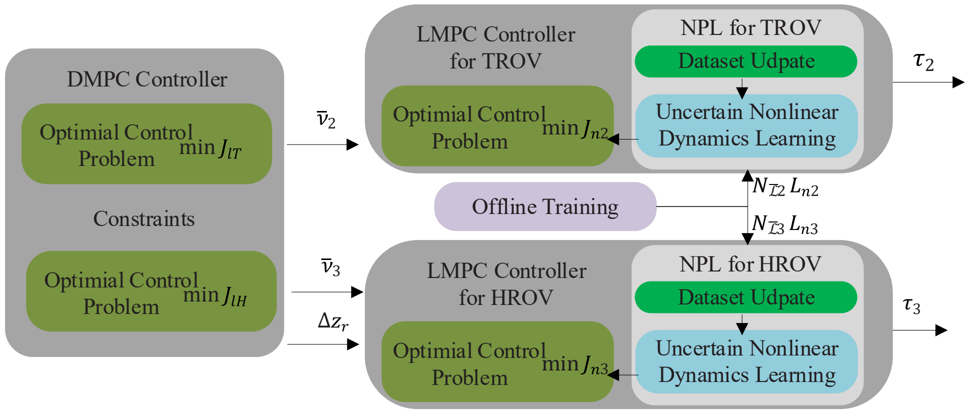

Fig. 3. Scheme of the cooperative control strategy.

where the nonlinear dynamics represents the interaction force between the MRT and seafloor sediments, the projection of the two-force member's internal force in the TROV's local coordinate frame and the nonlinear hydrodynamic force of the TROV.

$$g_2(\mathscr{X}_2) = \begin{bmatrix} \mathscr{J} & 0_{3\times1} \\ 0_{1\times3} & 0 \end{bmatrix} \left(\begin{bmatrix} -F_R\cos\delta \\ F_R\sin\delta \\ -\mathrm{sg}(\omega_1)M_{o_2} \\ 0 \end{bmatrix} + T_{link} \begin{bmatrix} \cos\phi\sin\theta\cos\psi_1 + \sin\phi\sin\psi_1 \\ \sin\phi\cos\psi_1 - \cos\phi\sin\theta\sin\psi_1 \\ 0 \\ 0 \end{bmatrix} \right) + \begin{bmatrix} (X_{vr}+m_2)v_2\omega_2 + X_{rr}\omega_2^2 + X_{uu}|u_2|u_2 \\ Y_{uv}u_2v_2 + (Y_{ur}-m_2)u_2\omega_2 + Y_{vv}|v_2|v_2 \\ N_{uv}u_2v_2 + N_{ur}u_2\omega_2 + \dfrac{I_1u_2^2\delta}{L^2} + N_{rr}|\omega_2|\omega_2 \\ 0 \end{bmatrix}, h_{e2} = \begin{bmatrix} \tau_{e2} \\ 0 \end{bmatrix} \tag{31}$$

Similarly, function $f_3(\mathscr{X}_3)$, also consists of the HROV's nonlinear dynamics function $g_3(\mathscr{X}_3)$, parametric uncertainty of the HROV's hydrodynamics $\tilde{g}_3$, and the unknown external ocean current disturbance h_{e3}:

$$f_3(\mathscr{X}_3) = \begin{bmatrix} \mathscr{M}_3^{-1} \\ 0_{1\times4} \end{bmatrix} \left(g_3(\mathscr{X}_3) + \tilde{g}_3 \right) + h_{e3} \tag{32}$$

where the nonlinear dynamics represent the projection of the two-force member's internal force in the HROV's local coordinate frame and the nonlinear hydrodynamic force of the HROV.

3. Cooperative control strategy

One control objective is for the TROV to tow the MRT along a reference path, while keeping the MRT's body subsidence at a special height above the sediment surface for efficient collection. Furthermore, the HROV need keep synchronization with the MRT to efficiently provide vertical tensile force via the two-force member.

Since the RDMV's dynamics are multi-DOF coupled and subject to hard equality constraint on the relative position relationship between HROV and ROV, constructing a single OCP to meet these control objectives may lead to poor real-time performance or even infeasibility. Then, a cooperative control strategy consisting of a DMPC controller and two LMPC controllers are developed, whose scheme is shown in Fig. 3.

The DMPC controller is developed to turn the strict equality constraint into the penalty term of the cost function. Then, OCPs are constructed separately to calculate the virtual speed control laws of the

$$g_3(\mathscr{X}_3) = \begin{bmatrix} (X'_{vr}+m_3)v_3\omega_3 + X'_{rr}\omega_3^2 + X'_{uu}|u_3|u_3 \\ Y'_{uv}u_3v_3 + (Y'_{ur}-m_3)u_3\omega_3 + Y'_{vv}|v_3|v_3 \\ N'_{uv}u_3v_3 + N'_{ur}u_3\omega_3 + N'_{rr}|\omega_3|\omega_3 \\ Z_{uw}u_3w + Z_{ww}|w|w \\ 0 \end{bmatrix} + T_{link} \begin{bmatrix} -\cos\phi\sin\theta\cos\psi_3 - \sin\phi\sin\psi_3 \\ -\sin\phi\cos\psi_3 + \cos\phi\sin\theta\sin\psi_3 \\ -\cos\phi\cos\theta \\ 0 \\ 0 \end{bmatrix}, \quad h_{e3} = \begin{bmatrix} \tau_{e3} \\ 0 \end{bmatrix} \tag{33}$$

TROV and the HROV to meet the control objectives. Given a vector $\eta_r = (x_{1r}, y_{1r}, \psi_{1r})^{\mathrm{T}}$ that stands for the reference path point. Given a vector $\eta_1 = (x_1, y_1, \psi_1)^{\mathrm{T}}$, the path tracking deviation is denoted by $e_{\eta 1} := (\eta_1 - \eta_{1r}; u_1 - u_{1r}) = (e_{x1}, e_{y1}, e_{\psi_1}, e_{u_1})^{\mathrm{T}}$. Given a vector $\eta_3 = (x_3, y_3, \psi_3)^{\mathrm{T}}$, and the synchronization deviation of the MRT and the HROV is denoted by $e_{\eta 3} := (\eta_3 - \eta_{3r}; u_3 - u_{3r}) = (e_{x3}, e_{y3}, e_{\psi 3}, e_{u3})^{\mathrm{T}}$.

Denote the velocity vectors of the MRT, TROV and HROV by $\nu_1 := (u_1, v_1, \omega_1)^{\mathrm{T}}$, $\nu_2 := (u_2, v_2, \omega_2)^{\mathrm{T}}$and $\nu_3 := (u_3, v_3, \omega_3)^{\mathrm{T}}$.The virtual speed control law of the TROV $\overline{\nu}_2$ can be obtained to converge path tracking deviation $e_{\eta 1}$, while the virtual speed control law of the $\overline{\nu}_3$ can be obtained to converge synchronization deviation $e_{\eta 3}$.

With the uncertain nonlinear dynamics of the RDMV learned through the proposed NPL method, a LMPC controller for the TROV is developed to calculate the control input τ_2 to track the virtual speed control laws $\overline{\nu}_2$. Moreover, to track the virtual speed control law $\overline{\nu}_3$ and maintain a certain MRT's body subsidence, a LMPC controller for the HROV is also developed to compute the control input τ_3.

3.1. DMPC controller

Considering the control objectives, the cost function of an optimal control problem can be designed as:

$$J_l = \sum_{i=0}^{N_l-1} \|e_{\eta 1}(i|k)\|_{Q_{l1}}^2 + \|e_{\eta 3}(i|k)\|_{Q_{l3}}^2 + \|\mathscr{U}_1(i|k)\|_{R_{l1}}^2 + \|\mathscr{U}_3(i|k)\|_{R_l}^2 + \|e_{\eta 1}(N_l|k)\|_{P_{l1}}^2 + \|e_{\eta 2}(N_l|k)\|_{P_{l3}}^2 \tag{34}$$

where denote the speed increments of the MRT and the HROV by $\mathscr{U}_1 := (\Delta u_1, \Delta v_1, \Delta \omega_1)^{\mathrm{T}}$ and $\mathscr{U}_3 := (\Delta u_3, \Delta v_3, \Delta \omega_3)^{\mathrm{T}}$. N_l is predictive horizon. Q_{l1}, R_{l1}, Q_{l3}, and R_{l3} are weight matrices. Denote terminal weight matrices by P_{l1} and P_{l3}. Since the HROV mainly provides vertical tensile force to keep the reference body subsidence of the MRT, Δz_r, the global z-axis coordinate of the HROV can be obtained from Eq. (2): $z_r := L_1 + h - \Delta z_r$.

Considering the speed increment of the MRT and the HROV, inequality constraints are introduced:

$$\begin{aligned} \mathscr{U}_1 &\in \mathbb{U}_{l1} := \{\mathscr{U}_1 | \mathscr{U}_{1\min} \le \mathscr{U}_1 \le \mathscr{U}_{1\max}\} \\ \mathscr{U}_3 &\in \mathbb{U}_{l3} := \{\mathscr{U}_3 | \mathscr{U}_{3\min} \le \mathscr{U}_3 \le \mathscr{U}_{3\max}\} \end{aligned} \tag{35}$$

where inequality constraints (33) are designed to satisfying the physical constraints of the speed increment.

To consider equality constraints of the RDMV's kinematic model, the discretized state space model of the MRT and the HROV is introduced:

$$\chi_1(k+1) = A_1(k)\chi_1(k) + B_1(k)\mathscr{U}_1(k), \chi_3(k+1) = A_3(k)\chi_3(k) + B_3(k)\mathscr{U}_3(k) \tag{36}$$

where the state of the MRT is denoted by $\mathscr{X}_1 := (\eta_1; \upsilon_1)$, and the state of the HROV $\mathscr{X}_3 := (\eta_3; \upsilon_3)$. The time-varying state matrices are denoted by A_1 and A_3. Denote the time-varying control matrices by B_1 and B_3:

$$A_1 = \begin{bmatrix} I_3 & T_l \mathscr{J}_1 \\ 0_{3\times 3} & I_3 \end{bmatrix}, A_3 = \begin{bmatrix} I_4 & T_l \mathscr{J}_3 \\ 0_{4\times 4} & I_4 \end{bmatrix}, B_3 = \begin{bmatrix} T_l \mathscr{J}_3 \\ I_4 \end{bmatrix} \tag{37}$$

where T_l is the sampling time. Denote the transformation matrices by $\mathscr{J}_1$ and $\mathscr{J}_3$:

$$\mathscr{J}_1 = \begin{bmatrix} \cos\psi_1 & -\sin\psi_1 & 0 \\ \sin\psi_1 & \cos\psi_1 & 0 \\ 0 & 0 & 1 \end{bmatrix}, \mathscr{J}_3 = \begin{bmatrix} \cos\psi_3 & -\sin\psi_3 & 0 & 0 \\ \sin\psi_3 & \cos\psi_3 & 0 & 0 \\ 0 & 0 & 1 & 0 \\ 0 & 0 & 0 & 1 \end{bmatrix} \tag{38}$$

Since the HROV and the MRT is articulated by a two-force member, an equality hard constraint on the relative position must be introduced:

$$d(x_1, x_3, y_1, y_3, z) = \sqrt{e_{p3}^2 + (z - h + \Delta z)^2} = L_1 \tag{39}$$

where the relative position of horizontal plane is denoted by $e_{p3} = \sqrt{(x_1 - x_3)^2 + (y_1 - y_3)^2}$.

Then, an optimal control problem is formulated to calculate the virtual speed control law of the MRT and the HROV

$$\begin{aligned} &\min_{\substack{\mathscr{U}_1(i|k), i\in\mathbb{K}_{0:N_l-1} \\ \mathscr{U}_3(i|k), i\in\mathbb{K}_{0:N_l-1}}} J_l \quad (40a) \\ \text{s.t.} \quad & \chi_1(0|k) = \chi_1(k),\ \mathscr{U}_1(0|k) = \mathscr{U}_1(k), \quad (40b) \\ & \chi_3(0|k) = \chi_3(k),\ \mathscr{U}_3(0|k) = \mathscr{U}_3(k), \\ & \chi_1(i+1|k) = A_1\chi_1(i|k) + B_1\mathscr{U}_1(i|k), \quad (40c) \\ & \chi_3(i+1|k) = A_3\chi_3(i|k) + B_3\mathscr{U}_3(i|k), \\ & \mathscr{U}_1(i|k) \in \mathbb{U}_{l1},\ \mathscr{U}_3(i|k) \in \mathbb{U}_{l3}, \quad (40d) \\ & d(x_1(i|k), x_3(i|k), y_1(i|k), y_3(i|k), z(i|k)) - L_1 = 0, \quad (40e) \end{aligned} \tag{40}$$

In the optimal control problem, the real-time performance may not be ensured due to three equality constraints and two inequality constraints. Besides, the feasibility of the optimal control problem is a challenge due to hard equality constraint on the relative position (40e).

To overcome the issues, a novel DMPC controller is developed to separately formulate the optimal control problem of the MRT and the HROV to calculate the virtual speed control law $\overline{\nu}_1$ and $\overline{\nu}_3$. For constraint on relative position (40e), it is transformed to a soft constraint, and the cost functions are reconstructed as that of J_{l1} for the MRT and J_{l3} for the HROV:

$$J_{l1} = \sum_{i=0}^{N_l-1} \|e_{\eta 1}(i|k)\|_{Q_{l1}}^2 + \|\mathscr{U}_1(i|k)\|_{R_{l1}}^2 + \|e_{\eta 1}(N_l|k)\|_{P_{l1}}^2 \tag{41}$$

$$J_{l3} = \sum_{i=0}^{N_l-1} \|e_{\eta 3}(i|k)\|_{Q_{l3}}^2 + \|\mathscr{U}_3(i|k)\|_{R_{l3}}^2 + \|e_{\eta 3}(N_l|k)\|_{P_{l3}}^2 \tag{42}$$

where weight matrices Q_{l1}, P_{l1}, Q_{l3} and P_{l3} are used for penalizing the MRT's path tracking deviation and the synchronization deviation. The weight matrices R_{l1} and R_{l3} are used for smooth change of the virtual speed control law.

Then, two optimal control problems are respectively formulated to calculate the virtual speed control law of the MRT and the HROV:

$$\begin{aligned} &\min_{\mathscr{U}_1(i|k), i\in\mathbb{K}_{0:N_l-1}} J_{l1} \quad (43a) \\ \text{s.t.} \quad & \chi_1(0|k) = \chi_1(k),\ \mathscr{U}_1(0|k) = \mathscr{U}_1(k), \quad (43b) \\ & \chi_1(i+1|k) = A_1\chi_1(i|k) + B_1\mathscr{U}_1(i|k), \quad (43c) \\ & \mathscr{U}_1(i|k) \in \mathbb{U}_{l1}, \quad (43d) \end{aligned} \tag{43}$$

$$\begin{aligned} &\min_{\mathscr{U}_3(i|k), i\in\mathbb{K}_{0:N_l-1}} J_{l3} \quad (44a) \\ \text{s.t.} \quad & \chi_3(0|k) = \chi_3(k),\ \mathscr{U}_3(0|k) = \mathscr{U}_3(k), \quad (44b) \\ & \chi_1(0|k) = \chi_1(k), \\ & \chi_3(i+1|k) = A_3\chi_3(i|k) + B_3\mathscr{U}_3(i|k), \quad (44c) \\ & \chi_1(i+1|k) = A_1\chi_1(i|k), \\ & \mathscr{U}_3(i|k) \in \mathbb{U}_{l3} \quad (44d) \end{aligned} \tag{44}$$

where the solutions to OCP (43) and OCP (44) are separately denoted by $\mathscr{U}_1^*(i|k)$and$\mathscr{U}_3^*(i|k)$, $i \in \mathbb{K}_{0:N_l-1}$. The virtual speed control laws of the MRT and the HROV can be obtained:

$$\overline{\nu}_1 = \mathscr{U}_1^*(0|k) + \upsilon_1(k), \overline{\nu}_3 = \mathscr{U}_3^*(0|k) + \upsilon_3(k) \tag{45}$$

Remark 1. At each time step, the time-varying state matrices and

Table 1
Literature review table.

Content	Article	Problem
Traditional MPC	[10,11]	Degradation of control performance from model mismatch
LMPC using neural network	[19–21]	Challenge of obtaining data for pre-training neural networks
LMPC using KI prediction function	[18,24]	Degradation of learning performance from Redundant sampling points

Table 2
Motion control performance.

Method	Average depth deviation (m)	Max depth deviation (m)	Average yaw angle deviation (°)	Max yaw angle deviation (°)
the proposed control strategy	< 0.01	0.01	0.05	0.01
control strategy in [38]	0.04	0.05	0.07	0.08

control matrices are assumed to be linear time-invariant at each time step. Then, optimal control problems (43) and (44) can be transformed into quadratic programming problems, which can be efficiently solved. The detailed derivations can be found in [37].

According to the kinematic model of RDMV, the TROV's virtual speed control law $\overline{\nu}_2$ can be calculated:

$$\overline{\nu}_2 = \quad (\overline{u}_2, \overline{v}_2, \overline{\delta})^{\mathrm{T}} = \left(\overline{u}_1 \cos\delta + \overline{v}_1 \sin\delta, \overline{v}_1 \cos\delta - \overline{u}_1 \sin\delta, \frac{\overline{\omega}_1}{\overline{u}_1} L_2 \right)^{\mathrm{T}} \tag{46}$$

3.2. Enhanced NPL method

As the scheme of the cooperative control strategy shown in Fig. 3, two OCPs are separately formulated to obtain the control inputs to track the virtual speed control laws. Since parametric uncertainties in the kinetic model and the unknown external ocean current disturbances lead to uncertain nonlinear dynamics f^2 and f^3, state space (27) can't be directly utilized as a state transition model in the optimal control problem. Based on KI prediction function [24], the enhanced NPL method is developed to estimate the actual values of the uncertain nonlinear dynamics subject to the random bounded process noise.

Denote the estimated value of the nonlinear dynamics by $\widehat{f}$, and the sampled data set utilized for calculating the estimated value is denoted by D_n

$$D_n := \left\{ \left(s(r), \widetilde{f}(s(r)) \right) | r \in \mathbb{K}_{1:N_n} \right\} \tag{47}$$

where $s(k) := (\chi(k), \mathscr{U}(k)) \in \mathbb{S} \subset \mathscr{R}^{(n_x+n_u)\times 1}$ represents the measured sampling point, with the total number of the sampling point denoted by N_n. $\mathbb{S}$ represents the input space. For convenience, $\mathscr{G}_n := \{s(r) | r \in \mathbb{K}_{1:N_n}\}$ represents the sampled input data set. The measured nonlinear dynamics are denoted by $\widetilde{f}(s(r)) := \chi(r) - A\chi(r-1) - B\mathscr{U}(r-1)$.

Definition 1. **(KI prediction function):** Based on the sampled data set, the map $\widehat{f}(s(k), L_n, D_n) : \mathbb{S} \rightarrow \mathbb{Y}$ is obtained by the KI prediction function:

Table 5
Performance of the two NPL methods.

	Proposed NPL Method	Comparative NPL Method
Number of the sample points	6	13
Mean square error	0.0856	0.1251
Simulation time (s)	82.27	123.18

Table 3
Parameters of the dynamic model of RDMV.

Parameter	Value	Parameter	Value	Parameter	Value
L_2	0.5 m	l	2 m	b	1.4 m
m_1	40.5 kg	m_2	48.85 kg	I_2	11.6 kgm^2
I_1	45.85 kgm^2	m_δ	4.12 kg	$X_{\dot{u}}$	−3.9 kg
$Y_{\dot{v}}$	−149.9 kg	$N_{\dot{r}}$	−53.87 kgm^2	X_u	−4.1 kg/m
N_r	−547 kgm^2/s/rad	Y_{vv}	−553.4 kg/m	X_{uu}	−8.2 kg
N_{rr}	−1037 kgm^2/s/rad	Y_v	−285.7 kg/m	X_{vr}	−149.9 kg
Y_{ur}	−120.8 kg	X_{rr}	−13.18 kgm/rad	Y_{uv}	−120.8 kg
N_{ur}	−13.6 kg	N_{uv}	−163.9 kg	E_1	0.95
E_2	−0.1	E_3	−0.1	CI	420
c	5.4 kPa	Φ	6.2 °	N_r	0.1
N_c	6.36	r_s	12.2 kN/m^3	L_1	0.4
W	244.5 N	Z_w	−233.7 kg/m	Z_{ww}	−533.4 kg/m
$Z_{\dot{w}}$	−149.9 kg	Z_{uw}	−22.05 kg		

Table 4
Parameters used in the optimal control problems.

Parameter	Value	Parameter	Value	Parameter	Value
Q_{l1}	$(44, 112, 1595, 305)^T$	P_{l1}	$(84, 272, 1895, 355)^T$	R_{l1}	$(500, 400, 100)^T$
Q_{l2}	$(384, 252, 5595, 8005)^T$	P_{l2}	$(564, 472, 7895, 9355)^T$	R_{l2}	
Q_{n2}	$(61, 90, 355)^{\mathrm{T}}$	P_{n2}	$(81, 98, 443)^{\mathrm{T}}$	Q_z	310
Q_{n2}	$(610, 900, 3555)^{\mathrm{T}}$	P_{n2}	$(810, 985, 4435)^{\mathrm{T}}$	P_z	510
T_l	0.05	T_n	0.05	R_{n2}	$(61, 200, 150)^T$
$\mathscr{U}_{3_{\max}}$	$(0.01, 0.03, 0.005)^T$	$\mathscr{U}_{1_{\min}}$	$(0.05, 0.01, 0.002)^T$	$\Delta U_{3_{\min}}$	$-\Delta U_{3_{\max}}$
$\mathscr{U}_{1_{\max}}$	$-\mathscr{U}_{1_{\min}}$	$U_{2_{\min}}$	$-(40, 80, 85)^{\mathrm{T}}$	$\mathscr{U}_{3_{\max}}$	$-\mathscr{U}_{3_{\min}}$
$U_{3_{\max}}$	$(30, 70, 85, 80)^{\mathrm{T}}$	$\Delta U_{2_{\max}}$	$(10, 3, 5)^{\mathrm{T}}$	$U_{2_{\max}}$	$(30, 80, 85)^{\mathrm{T}}$
$U_{3_{\min}}$	$-(40, 80, 85, 80)^{\mathrm{T}}$	$\Delta U_{3_{\max}}$	$(10, 2, 3, 15)^{\mathrm{T}}$	$\Delta U_{2_{\min}}$	$-\Delta U_{2_{\max}}$
N_n	7	N_l	6		

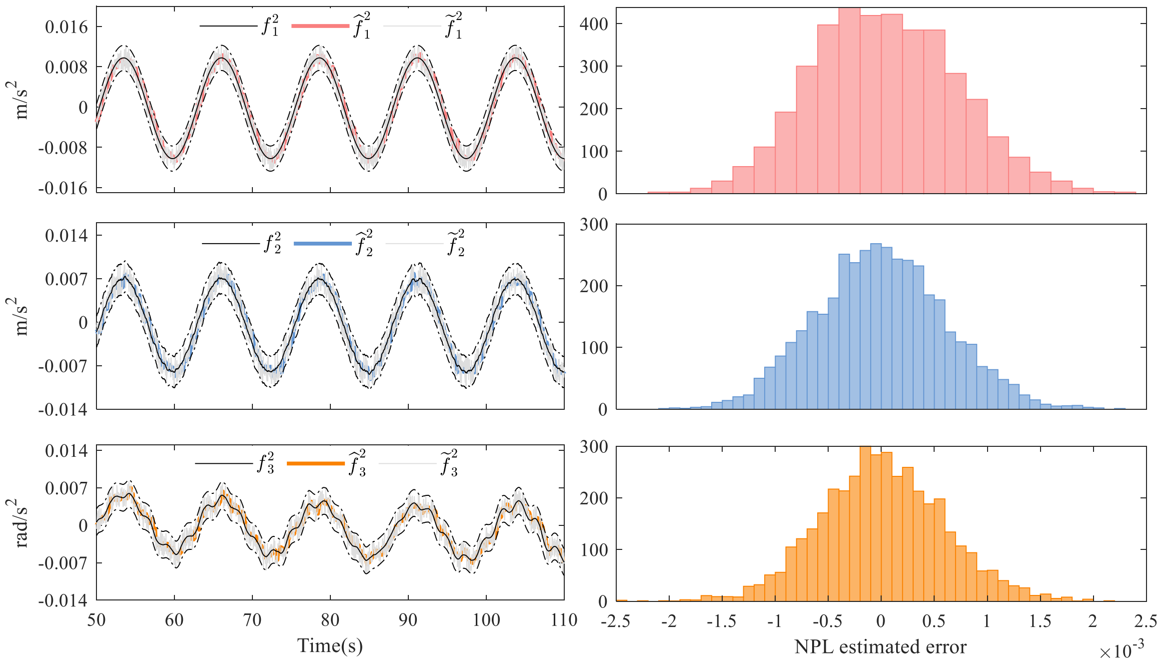

Fig. 4. Results of the learned TROV's uncertain nonlinear dynamics function (comparison of the reference values with noise, the estimated values and the actual values (left) and results of histogram (right) of the NPL estimated error).

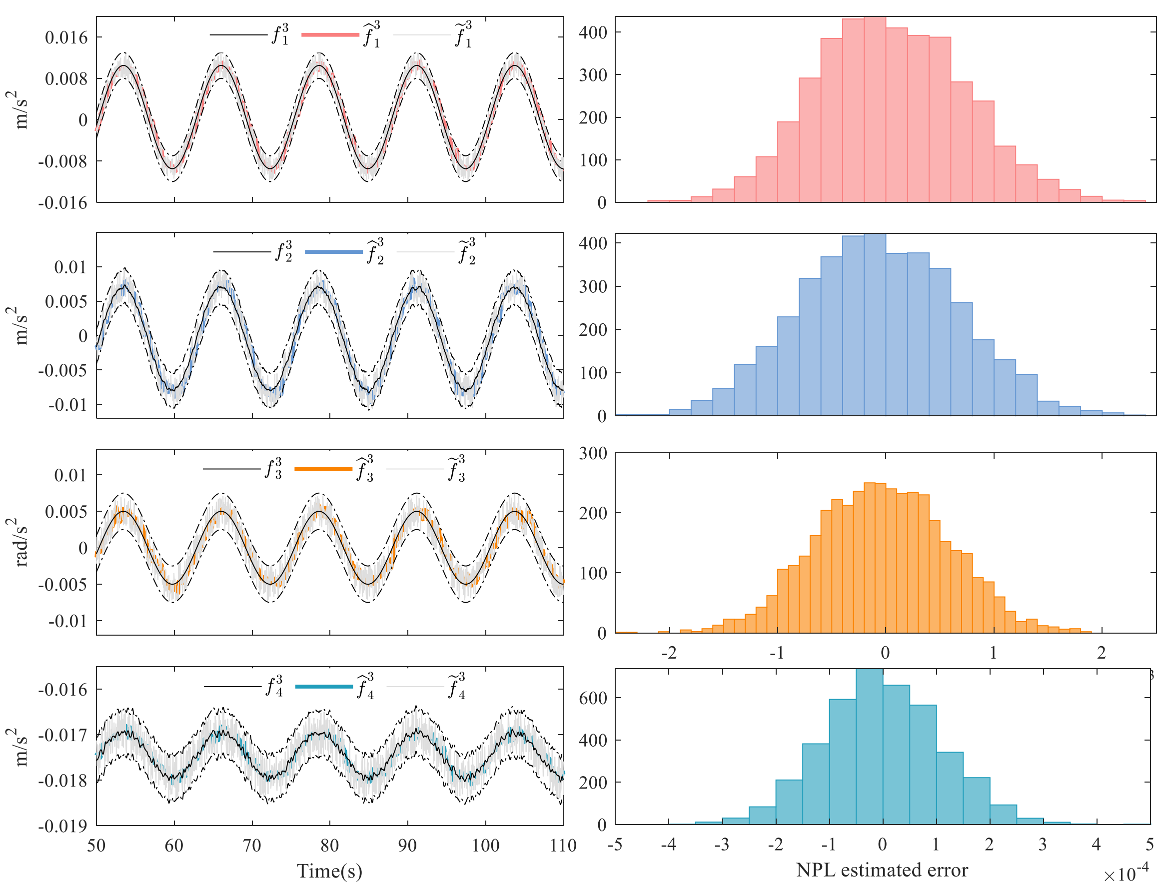

Fig. 5. Results of the learned HROV's uncertain nonlinear dynamics (comparison of the reference values, the estimated values and the actual values with noise (left) and results of histogram (right) of the NPL estimated error).

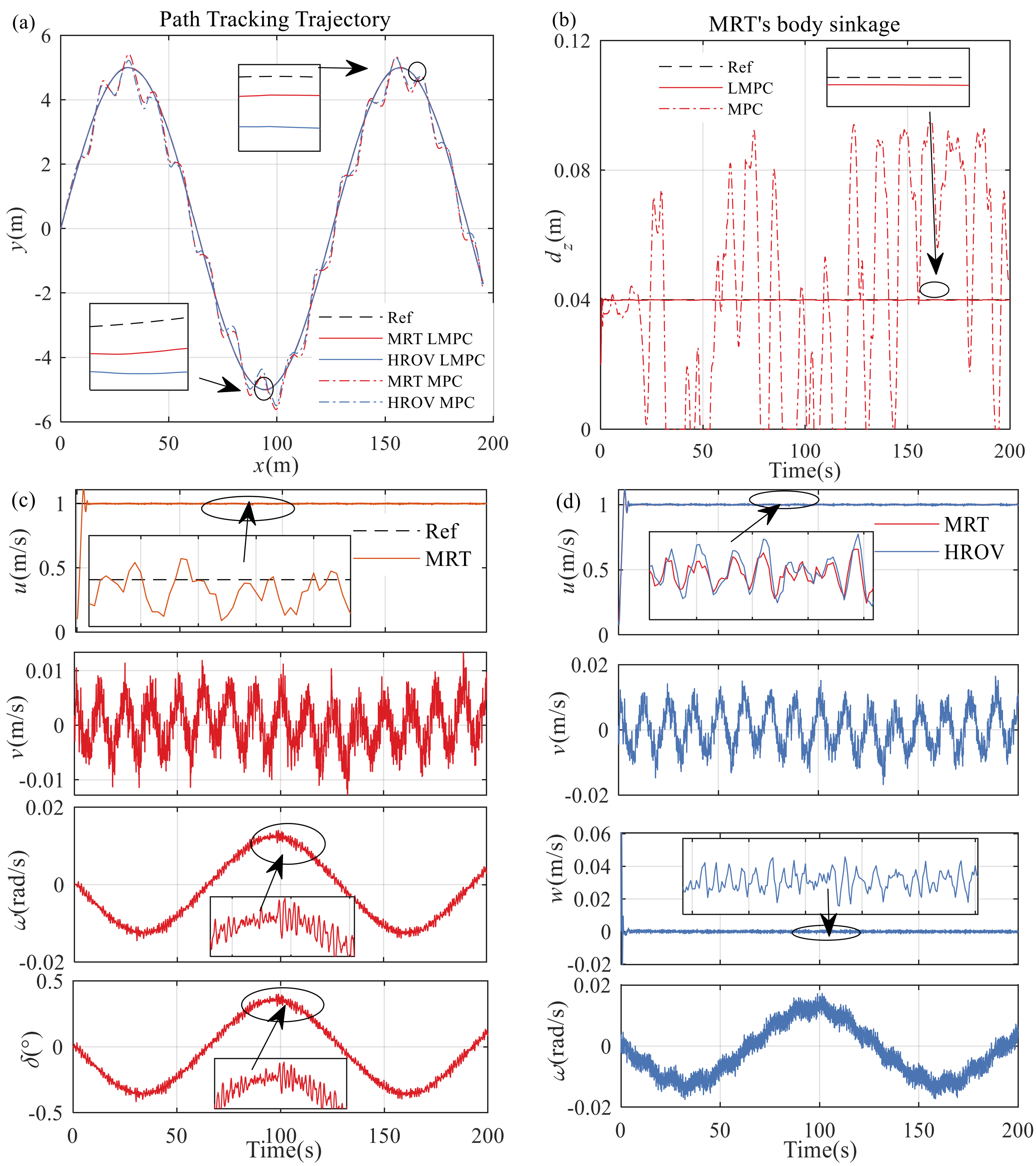

Fig. 6. Control trajectory of the proposed cooperative control strategy (LMPC) and the strategy in comparative numerical simulation (MPC). (a) Trajectory of the RDMV, where the solid line represents the horizontal plane coordinate of the MRT and the HROV, and the dot dash line represents the MRT and the HROV's horizontal plane coordinates in the comparative numerical simulation (MPC). (b) the MRT's body sinkage using the proposed cooperative control strategy. (c) the MRT 's state and the horizontal rotation angle of the TROV using the proposed cooperative control strategy. (d) the HROV's state using the proposed cooperative control strategy.

Table 6
Reset parameters used in the MPC controller.

Parameter	Value	Parameter	Value	Parameter	Value
Q_{n2}	$(43, 30, 355)^T$	P_{n2}	$(34, 58, 843)^T$	Q_z	610
Q_{n2}	$(513, 700, 5555)^T$	P_{n2}	$(412, 751, 4612)^T$	P_z	1010
R_{n2}	$(31, 100, 452)^T$				

Table 7
Evaluation metrics for MRT's path tracking.

Control Strategy	MRT's Average path tracking deviation (m)	MRT's Max path tracking deviation(m)
MPC	0.09	0.26
LMPC	0.01	0.02

Table 8
Evaluation metrics for HROV's horizontal synchronization and MRT's body sinking.

Control Strategy	MRT's average sinkage deviation (m)	MRT's Max sinkage deviation (m)	HROV's average synchronization deviation(m)	HROV's max synchronization deviation(m)
MPC	0.02	0.04	0.08	0.24
LMPC	0.01	0.02	< 0.01	0.01

$$\widehat{f}_j(s(k), L_n, D_n) := \frac{1}{2}\left(u_j\left(\widetilde{f}_j(s(r)), s(k), L_n, N_n\right) + \ell_j\left(\widetilde{f}_j(s(r)), s(k), L_n, N_n\right)\right), j \in \mathbb{K}_{1:n_x} \tag{48}$$

$$u\left(\widetilde{f}_j(s(r)), s(k), L_n, N_n\right) := \min_{r\in\mathbb{K}_{1:N_n}} \widetilde{f}_j(s(r)) + L_n\|s(k) - s(r)\|_\infty + \overline{\varepsilon} \tag{49}$$

$$\ell\left(\widetilde{f}_j(s(r)), s(k), L_n, N_n\right) := \max_{r\in\mathbb{K}_{1:N_n}} \widetilde{f}_j(s(r)) - L_n\|s(k) - s(r)\|_\infty - \overline{\varepsilon} \tag{50}$$

where L_n is the offline estimated Lipschitz constant based on the LACKI scheme [24]. $\mathbb{Y}$ represents the output space of the nonlinear dynamics: $f \in \mathbb{Y}\subset\mathscr{R}^{n_x\times 1}$.

Definition 2. **(minimal input space):** A space $\mathscr{L}\subset\mathbb{S}$ contains all possible sample points denotes the minimal input space, where the minimum number of sample points are denoted by $N_{\mathscr{L}}$.

Remark 2. The computational burden of the KI prediction function is related to the number of recorded samples N_n. To achieve good real-time performance, the nominal minimum number of sample points $N_{\overline{\mathscr{L}}}$ is obtained offline, and then the nominal minimal input space is denoted by $\overline{\mathscr{L}}\subset\mathbb{S}$.

Learning rule: The sampled data set $D_{N_{\overline{\mathscr{L}}}}$, formulated from the measured sampling point and the measured nonlinear dynamic, is updated over time:

$$D_{N_{\overline{\mathscr{L}}}} = \left\{\left(s(r), \widetilde{f}(s(r))\right) | r \in \mathbb{K}_{k-N_{\overline{\mathscr{L}}}+1:k}\right\} \tag{51}$$

3.3. LMPC controller

Since the nonlinear dynamics function $f_2(\chi_2)$ and $f_3(\chi_3)$ can be learned by the enhanced NPL method, the state transition models utilized in the optimal control problems are given as:

$$\begin{aligned}\mathscr{X}_2(k+1) &= \mathscr{A}_2\mathscr{X}_2(k) + \mathscr{B}_2U_2(k) + \widehat{f}^2(s_2(k), L_{n2}, D_{N_{\overline{\mathscr{L}}2}}),\\ \mathscr{X}_3(k+1) &= \mathscr{A}_3\mathscr{X}_2(k) + \mathscr{B}_3U_3(k) + \widehat{f}^3(s_3(k), L_{n3}, D_{N_{\overline{\mathscr{L}}3}})\end{aligned} \tag{52}$$

where the extended state is denoted by $s_2(k) = (\mathscr{X}_2(k), U_2(k))$, $s_3(k) = (\mathscr{X}_3(k), U_3(k))$.

To minimize the TROV's virtual speed deviation with smooth control input, a cost function J_{n2} is designed as follows:

$$J_{n2} = \sum_{i=0}^{N_n-1}\|e_{\nu2}(i|k)\|^2_{Q_{n2}} + \sum_{i=0}^{N_n-2}\|\Delta U_2(i|k)\|^2_{R_{n2}} + \|e_{\nu2}(N_n|k)\|^2_{P_{n2}} \tag{53}$$

where N_n is the predictive horizon. Q_{n2} and R_{n2} are weight matrices. $e_{\nu2} := \nu_2 - \overline{\nu}_2$ represents the virtual speed deviation of the HROV. Denote terminal weight matrix in the LMPC controller by P_{n2}. Weight matrices Q_{n2} and P_{n2} are used for penalizing the virtual speed deviation, and weight matrix R_{n2} are used to obtain smooth control input.

To satisfy the physical constraints of the TROV's control input increment and its maximum value, an inequality constraint is designed:

$$(U_2, \Delta U_2) \in \mathbb{U}_{n2} := \left\{(U_2, \Delta U_2) | U_{2_{\min}} \le U_2 \le U_{2_{\max}}, \Delta U_{2_{\min}} \le \Delta U_2 \le \Delta U_{2_{\max}}\right\} \tag{54}$$

where ΔU_2 denotes the control input increment of the TROV.

Then, an optimal control problem is formulated to calculate the TROV's control input:

$$\begin{aligned}&\min_{U_2(i|k), i\in\mathbb{K}_{0:N_n-1}} J_{n2}\\ &\mathscr{X}_2(0|k) = \mathscr{X}_2(k), U_2(0|k) = U_2(k)\\ \text{s.t.}\quad &\mathscr{X}_2(i+1|k) = \mathscr{A}_2\mathscr{X}_2(i|k) + \mathscr{B}_2U_2(i|k) + \widehat{f}(s_2(i|k), L_{n2}, D_{N_{\overline{\mathscr{L}}2}})\\ &\{U_2(i|k), \Delta U_2(i|k)\} \in \mathbb{U}_{n2}\end{aligned} \tag{55}$$

where the solution to the optimal control problem is denoted by $U_2^*(i|k)$, $i \in \mathbb{K}_{0:N_{n2}-1}$. Then, the TROV's control input can be obtained: $\tau_2(k) = U_2^*(0|k)$.

Note that a certain MRT's body sinkage can be transformed into the HROV's reference global z-axis coordinate based on Eq.2, and a cost function is designed to minimize the HROV's virtual speed deviation and track the HROV's reference global z-axis while ensuring smooth control input:

$$J_{n3} = \sum_{i=0}^{N_n-1}\|e_{\nu3}(i|k)\|^2_{Q_{n3}} + \|e_z(i|k)\|^2_{Q_z} + \sum_{i=0}^{N_n-2}\|\Delta U_3(i|k)\|^2_{R_{n3}} + \|e_{\nu3}(N_n|k)\|^2_{P_{n3}} + \|e_z(N_n|k)\|^2_{P_z} \tag{56}$$

where Q_{n3}, Q_z, Q_z and R_{n3} are weight matrices. P_z is the terminal weight matrix. $e_{\nu3} := \nu_3 - \overline{\nu}_3$ represents the virtual speed deviation of the HROV. Denote the HROV's z-axis coordinate deviation by $e_z := z - z_r$. Similarly, weight matrices Q_{n3} and P_{n3} are also used for penalizing the virtual speed deviation, and weight matrix R_{n2} are used to obtain smooth control input. Q_z and P_z are used for penalizing the HROV's z-axis coordinate deviation. Constraints on the control input and the HROV's speed are also considered as:

$$(U_3, \Delta U_3) \in \mathbb{U}_{n3} := \left\{(U_3, \Delta U_3) | U_{3_{\min}} \le U_3 \le U_{3_{\max}}, \Delta U_{3_{\min}} \le \Delta U_3 \le \Delta U_{3_{\max}}\right\} \tag{57}$$

where ΔU_3 denotes the control input increment of the HROV. Inequality constraint (55) is also designed to satisfy the physical constraints of the HROV's control input increment and its maximum value.

Then, an optimal control problem is formulated to calculate the HROV's control input:

$$\begin{aligned}&\min_{U_2(i|k), i\in\mathbb{K}_{0:N_n-1}} J_{n3}\\ &\mathscr{X}_3(0|k) = \mathscr{X}_3(k), U_3(0|k) = U_3(k)\\ \text{s.t.}\quad &\mathscr{X}_3(i+1|k) = \mathscr{A}_3\mathscr{X}_3(i|k) + \mathscr{B}_3U_3(i|k) + \widehat{f}(s_3(i|k), L_{n3}, D_{N_{\overline{\mathscr{L}}3}})\\ &\{U_3(i|k), \Delta U_3(i|k)\} \in \mathbb{U}_{n3}\end{aligned} \tag{58}$$

where the solution to the optimal control problem is denoted by $U_3^*(i|k)$,

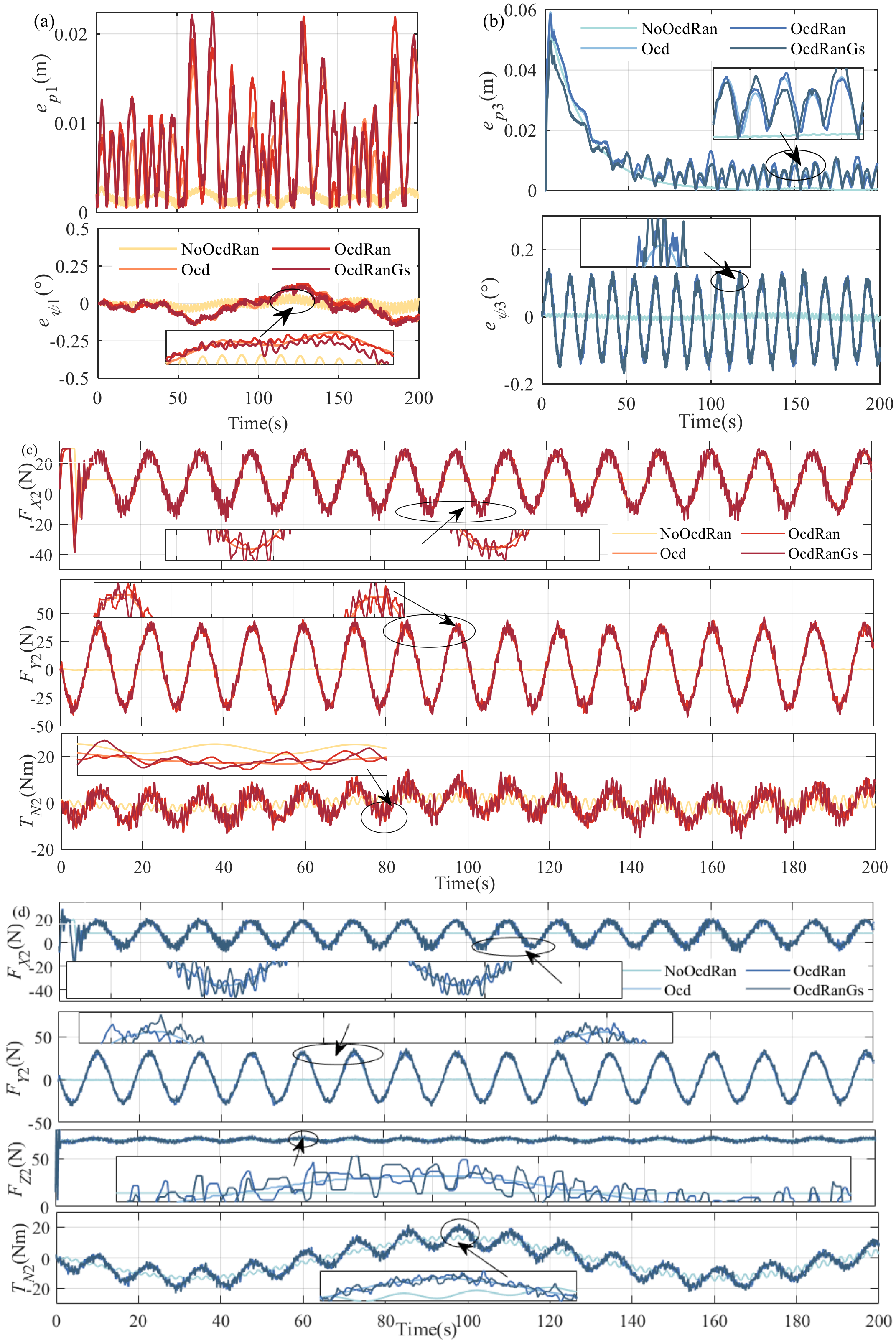

Fig. 7. Robust analysis results under the different environmental disturbance cases using the proposed cooperative control strategy, where denote the case with the ocean current disturbance and the uniformly distributed random noise by "OcdRan", and the case with the ocean current disturbance and the non-zero mean (Gaussian distributed) random noise by "OcdRanGs". The case only with the ocean current disturbance is denoted by "Ocd". The case without the ocean current disturbance and the random noise is denoted by "NoOcdRan". (a) range of the MRT's path tracking deviation, where the position deviation is denoted by $e_{p1} = \sqrt{e_{x1}^2 + e_{y1}^2}$. (b) range of synchronization deviation. (c) control input of the TROV. (d) control input of the HROV.

Table 9
Real-time performance evaluation of the LMPC controller.

	Average computing time (ms)	Max computing time (ms)
MPC−2	11.38	14.74
LMPC−2	12.14	15.85
MPC−3	12.87	15.21
LMPC−3	13.14	15.85

$i \in \mathbb{K}_{0:N_n-1}$. Then, the HROV's control input can be obtained: $\tau_3(k) = U_3^*(0|k)$.

3.4. Theoretical analysis

In Section 3.2, the enhanced NPL method estimates the nonlinear dynamics in the minimum input space, and the boundedness analysis of the estimation deviation is given as follows.

Assumption 1. The nonlinear dynamics f is always Lipschitz continuous as:

$$\forall x, y \in \mathbb{K}_{1:N_n}, \|f(s(x)) - f(s(y))\|_\infty \le L^* \|s(x) - s(y)\|_\infty$$

where L^* represents the bounded Lipschitz constant: $L^* \le \overline{L}^*$. The upper bound is denoted by $\overline{L}^*$.

Lemma 1. (Lipschitz Continuity) and Lemma 2 (Sample-consistency) are given for the following analysis:

Lemma 1. **(Lipschitz Continuity, [24]):** The KI prediction function $\widehat{f}(s(k), L_n, D_n)$ is also Lipschitz continuous:

$$\forall x, y \in \mathbb{K}_{1:N_n}, \|\widehat{f}(s(x), L_n, D_n) - \widehat{f}(s(y), L_n, D_n)\|_\infty \le L_n \|s(x) - s(y)\|_\infty \tag{59}$$

Lemma 2. **(Sample-consistency, [24]):** The KI prediction function is sample-consistent (up to $\frac{\lambda}{2}$) in the minimum input space $\mathscr{L}$, and the NPL estimated error $\|f - \widehat{f}\|_\infty$ is bounded:

$$\forall r \in \mathbb{K}_{1:N_n}, \widehat{f}(s(r), L_n, D_n) \in \mathscr{B}_{\frac{\lambda}{2}}\left(\widetilde{f}(s(r))\right) \tag{60}$$

$$\|f(s(r)) - \widehat{f}(s(r), L_n, D_n)\|_\infty \le \frac{\lambda}{2} + \overline{\varepsilon} \tag{61}$$

where $\mathscr{B}_{\frac{\lambda}{2}}\left(\widetilde{f}(s(r))\right) = \left\{ y \in \mathbb{Y} \left\| y - \widetilde{f}(s(r)) \right\|_\infty \le \frac{\lambda}{2} \right\}$ denotes the $\frac{\lambda}{2}$-ball around the measured output.

Since the enhanced NPL method estimates the nonlinear dynamics in the nominal minimum input space, the corresponding boundedness analysis of the NPL estimated error is given as follows.

Definition 2. **(ε-convergent, [18]):** A point set $\mathscr{s}_{\mathbb{N}} = \{s(r) | r \in \mathbb{K}_{1:\mathbb{N}}\}$ is ε-convergent to a point $s(r^*) \in \mathbb{S}$by $\mathscr{s}_{\mathbb{N}} \xrightarrow{\varepsilon} s(r^*)$: iff $\exists m \in \mathbb{K}_{1:\mathbb{N}}$, $\forall r > m$, $\|s(r) - s(r^*)\|_\infty \le \varepsilon$, where ε is a positive constant.

Definition 3. **(ε-denseness, [18]):** Denote a set sequence $\mathscr{S}_{\mathbb{N}} = \{\mathscr{s}_r | r \in \mathbb{K}_{1:\mathbb{N}}\}$ ε-dense to a point $s(r^*) \in \mathscr{s}_{\mathbb{N}}$ by $\mathscr{S}_{\mathbb{N}} \xrightarrow{\varepsilon} s(r^*)$: if $\exists n \in \mathbb{K}_{1:\mathbb{N}}$, $\mathscr{s}_n \xrightarrow{\varepsilon} s(r^*) \wedge \mathscr{s}_n \in \mathscr{S}_{\mathbb{N}}$. Denote a set sequence $\mathscr{S}_{\mathbb{N}}$ ε-dense to a point set $\mathscr{s}_{\mathbb{N}}$ by $\mathscr{S}_{\mathbb{N}} \xrightarrow{\varepsilon} \mathscr{s}_{\mathbb{N}}$: $\forall s(r^*) \in \mathscr{s}_{\mathbb{N}} : \mathscr{S}_{\mathbb{N}} \xrightarrow{\varepsilon} s(r^*)$, where ε is a positive constant.

Before giving the boundedness analysis of the estimation deviation, a probability space is defined. The sample space Ω denotes collection of all possible sequences $\mathscr{S}_{\mathbb{N}}$. The event space F denotes a ε-algebra containing subsets of the sample space related to two definitions ε-convergent and ε-denseness. Probability measure P denotes the function assigning probabilities to each event in the event space.

Theorem 1. The nominal minimal input space $\overline{\mathscr{L}}$ is $\varepsilon_{\overline{\mathscr{L}}}$-dense to the minimal input space $\mathscr{L}$:

$$\mathrm{P}(\overline{\mathscr{L}} \overset{\varepsilon_{\overline{\mathscr{L}}}}{\to} \mathscr{L}) = 1 \tag{62}$$

where the hyper-parameter $\varepsilon_{\overline{\mathscr{L}}}$ satisfies $\varepsilon_{\overline{\mathscr{L}}} = p/L_n > \varepsilon^*$.

Proof. Given a ball around $s(k)$ as: $\mathscr{B}_{\varepsilon^*}(s(k)) = \{s(r) \in \mathbb{S} \| s(k) - s(r)\|_\infty \le \varepsilon^*\}, k, r \in \mathbb{K}_{k-N_{\overline{\mathscr{L}}}+1:k}$. For the nominal minimal input space, based on LACKI scheme [24], a larger $\overline{\mathscr{L}}$-ball exists:

$$\mathscr{B}_{\varepsilon^*}(s(k)) \subset \mathscr{B}_{\varepsilon_{\overline{\mathscr{L}}}}(s(k)) = \{s(r) \in \mathbb{S} \| s(k) - s(r)\|_\infty \le \varepsilon_{\overline{\mathscr{L}}}\}, k \in \mathbb{K}_{k-N_{\overline{\mathscr{L}}}+1:k}, r \in \mathbb{K}_{k-N_{\mathscr{L}}+1:k} \tag{63}$$

In Definition 3, $\overline{\mathscr{L}} \xrightarrow{\varepsilon_n} \mathscr{L}$ can be expressed as:

$$\forall s \in \mathscr{L}, \exists m \in \mathbb{K}_{k-N_{\mathscr{L}}+1:k}, \forall r > m : \mathrm{dist}(\overline{\mathscr{L}}, r) \le \varepsilon_{\overline{\mathscr{L}}} \tag{64}$$

where $\mathrm{dist}(\overline{\mathscr{L}}, s)$ is denoted by: $\mathrm{dist}(\overline{\mathscr{L}}, r) = \min_{s^* \in \overline{\mathscr{L}}} \|s^* - s(r)\|_\infty$, $r \in \mathbb{K}_{k-N_{\mathscr{L}}+1:k}$, and contradiction is utilized to proof inequality (64). An assumption is given as:

$$\exists s^* \in \mathscr{L}, \forall m \in \mathbb{K}_{k-N_{\mathscr{L}}+1:k}, \exists r > m : \mathrm{dist}(\overline{\mathscr{L}}, r) > \varepsilon_{\overline{\mathscr{L}}} \tag{65}$$

It means no sample point contains in the $\varepsilon_{\overline{\mathscr{L}}}$-ball around s^*.That is $\mathscr{B}_{\varepsilon_{\overline{\mathscr{L}}}}(s(k)) \cap \overline{\mathscr{L}} = \phi$, and a probability is given:

$$p_r(s^*) = \mathrm{P}(s(r) \in \mathscr{B}_{\varepsilon_{\overline{\mathscr{L}}}}(s(k))), r \in \mathbb{K}_{k-N_{\overline{\mathscr{L}}}+1:k} \tag{66}$$

Then, inequality (66) is equivalent to

$$\mathrm{P}(\mathscr{B}_{\varepsilon_{\overline{\mathscr{L}}}}(s(k)) \cap \overline{\mathscr{L}} = \phi) = \prod_{r=k-N_{\overline{\mathscr{L}}}+1}^{k} (1 - p_r(s^*)) \tag{67}$$

The probability $p_r(s^*)$ is always nonnegative: $p_r(s^*) > 0$, Eq. (66) satisfies:

$$\lim_{\overline{\mathscr{L}} \to \infty} \mathrm{P}(\mathscr{B}_{\varepsilon_{\overline{\mathscr{L}}}}(s(k)) \cap \overline{\mathscr{L}} = \phi) = 0 \tag{68}$$

which means the assumption fails. Then, the proof completes. □

To analyze the conservative bound of the NPL estimated error, **Lemma 4** is given:

Lemma 3. [18]: Given a sample point $s \in \overline{\mathscr{L}}$, it holds that:

$$\ell_j\left(\widetilde{f}_j(r), s(k), L_n, N_{\mathscr{L}}\right) \le \widetilde{f}_j(s(\xi)) + L_n \|s(\xi) - s(r)\|_\infty + \overline{\varepsilon}, r \in \mathbb{K}_{k-N_{\mathscr{L}}+1:k} \tag{69}$$

where $\xi = \mathrm{argmin}_{\xi \in \overline{\mathscr{L}}} \|s(\xi) - s(r)\|_\infty, r \in \mathbb{K}_{k-N_{\mathscr{L}}+1:k}$ represents the nearest sample point in the nominal minimal input space.

Theorem 2. For the minimal input space $\mathscr{L}$, the NPL estimated error satisfies:

$$\|f(s(r)) - \widehat{f}(s(k), L_n, D_{\mathscr{L}})\|_\infty \le \frac{L_n + L^*}{L_n} p + 2\overline{e}, r \in \mathbb{K}_{k-N_{\mathscr{L}}+1:k} \tag{70}$$

Under the **Learning Rule**, the NPL estimated error in inequality (70) still holds.

Proof. : for the nearest sample point $s(\xi) \in \mathscr{L}$, it holds:

$$u\left(\widetilde{f}_j(r), s(k), L_n, N_{\mathscr{L}}\right) \le \widetilde{f}_j(s(\xi)) + L_n\|s(\xi) - s(r)\|_\infty + \overline{e}, r \in \mathbb{K}_{k-N_{\mathscr{L}}+1:k} \tag{71}$$

From Lemma 3, it holds:

$$\begin{aligned}\widehat{f}_j(s(k), L_n, D_{\mathscr{L}}) &= \frac{1}{2}\left(u_j\left(\widetilde{f}_j(r), s(k), L_n, N_{\mathscr{L}}\right) + \ell_j\left(\widetilde{f}_j(r), s(k), L_n, N_{\mathscr{L}}\right)\right) \\ &\le \widetilde{f}_j(s(\xi)) + L_n\|s(\xi) - s(r)\|_\infty + \overline{e}, r \in \mathbb{K}_{k-N_{\mathscr{L}}+1:k}\end{aligned} \tag{72}$$

which is equivalent to:

$$\left\|\widehat{f}_j(s(k), L_n, D_{\overline{\mathscr{L}}}) - \widetilde{f}_j(s(\xi))\right\|_\infty \le L_n\|s(\xi) - s(r)\|_\infty + \overline{e}, r \in \mathbb{K}_{k-N_{\mathscr{L}}+1:k} \tag{73}$$

Combining the bounded process noise $\left\|\widetilde{f} - f\right\|_\infty \le \overline{e}$ and Assumption 1, it holds that:

$$\left\|\widetilde{f}_j(s(\xi)) - f(s(k))\right\|_\infty \le L^*\|s(\xi) - s(r)\|_\infty + \overline{e}, r \in \mathbb{K}_{k-N_{\mathscr{L}}+1:k} \tag{74}$$

Based on triangle inequality, sum inequalities (73) and (74):

$$\begin{aligned}\|f(s(k)) - \widehat{f}(s(k), L_n, D_{\mathscr{L}})\|_\infty &\le (L^* + L_n)\|s(\xi) - s(r)\|_\infty + 2\overline{e} \\ &\le \frac{L_n + L^*}{L_n} p + 2\overline{e}, r \in \mathbb{K}_{k-N_{\mathscr{L}}+1:k}\end{aligned} \tag{75}$$

where the second inequality holds in Theorem 1.

Under the **Learning Rule,** inequality (71) holds by providing $\overline{\mathscr{L}} \xrightarrow{\varepsilon_{\overline{\mathscr{L}}}} \mathscr{L}$, and the nominal minimal input space $\overline{\mathscr{L}}$ is $\varepsilon_{\overline{\mathscr{L}}}$-dense to the input space $\mathscr{L}$ in Theorem 1. Then, the proof is completed.

Remark 3. The closed-loop stability of the RDMV system using the cooperative control strategy can be ensured by the stability of the DMPC controller and LMPC controller, which is affected by the solution to optimal control problems (43), (44), (55) and (58) without terminal constraints. For this kind of the optimal control problem, choosing appropriate terminal constraints and horizons can ensure its closed-loop stability. Similar stability analysis can be found in [18]. Note that the stability of the LMPC controller also suffers from the model mismatch such as the parameter uncertainty and the external disturbance, and the enhanced NPL method is proposed to obtain the accurate control-oriented model. Thus, the appropriate set of the hyper-parameters of the KI prediction function is also important for maintaining the stability of the LMPC controller.

4. Results and discussion

Based on the kinematic model and the discretized state space model, a discrete RDMV model can be obtained as the controlled object, with sampling period all set as 0.05 s. To verify the cooperative control strategy's superior robustness against model mismatch, a complex unknown external ocean current disturbance, which combines the disturbance related to the speed and the time varying sinusoidal disturbance, is introduced. Besides, the model mismatch from parametric uncertainty is modeled as $\widetilde{g}_2 = 0.1g_2, \widetilde{g}_3 = 0.1g_3$.

$$h_{e2} = \begin{cases} 0.1 * u_2^2 + 0.2 * \sin(0.4t) \\ v_2 + 0.15 * \sin(0.4t) \\ \omega_2^2 + 0.1 * \sin(0.4t) \\ 0 \end{cases}, h_{e2} = \begin{cases} 0 \\ 0 \\ 0.1 * w^2 + 0.01 * \sin(0.4t) \\ 0 \end{cases} \tag{76}$$

The unknown bounded process noise of the TROV is defined as: $w_2 = \left(w_2^1, w_2^2, w_2^3, 0\right)^{\mathrm{T}}$. That of the HROV is defined as: $w_3 = \left(w_3^1, w_3^2, w_3^3, w_3^4, 0\right)^{\mathrm{T}}$, w_2^1, w_2^2, w_3^3, w_3^1, w_3^2, $w_3^3 \in T * [-0.05, 0.05]$, $w_3^4 \in T * [-0.01, 0.01]$. Set the sampling period in the numerical simulations by $T = 0.05$s.

Note that the model mismatch from parametric uncertainty and the external ocean current disturbance are all unknown in the LMPC controllers, and the enhanced NPL is utilized to estimate the nonlinear dynamics function to obtain the accurate state transition models used in the LMPC controllers. To validate the superiority of the proposed enhanced NPL method, a comparative numerical simulation was carried out, where a nominal model predictive control (MPC) controller is utilized to replace the LMPC controller. The primary distinction in the simulation is the absence of a strategy to handle model mismatches. Then, numerical simulations are conducted to evaluate the learning performance of the enhanced NPL method and verify the control performance of the cooperative control strategy, which are carried out using Matlab, with AMD Ryzen Threadripper PRO 3995WX 64-Cores 2.70Ghz CPU and 256 GB RAM running Windows 10. The reference path of the MRT is generated by a sine curve:

$$\begin{cases} x_r = t \\ y_r = 5\sin 0.05t \\ \psi_r = \arctan(0.25\cos(0.05t)) \\ u_r = 1 \\ d_{zr} = 0.04 \end{cases} \tag{77}$$

where d_{zr} is the reference value of the MRT's body sinkage.

To visually demonstrate the control performance, the following three performance metrics are given. The MRT's path tracking deviation is denoted by $e_{p1} = \sqrt{e_{x1}^2 + e_{y1}^2}$, and the MRT's sinkage deviation is denoted by $e_z = d_z - d_{zr}$. Similarly, the HROV's synchronization deviation is denoted by $e_p = \sqrt{e_{x3}^2 + e_{y3}^2}$.

4.1. Method validation based on a degenerated individual ROV model

The validation of the RDMV model and its cooperative control strategy are crucial to the feasibility of the research. However, the deep-sea mining system studied in this paper is a kilometer complex giant system, even the underwater mining system is not easy to establish an experimental model. Due to limited experimental conditions and funding, this paper uses the results of a degraded ROV model in the existing literature [38] to verify the proposed LMPC controller. The depth control and the yaw angle control using the proposed LMPC controller are conducted under the complex unknown external ocean current disturbance. An optimal control problem similar to (43) is formulated to obtain the ROV's virtual speed control law, and an optimal control problem similar to (55) is formulated to track the speed control law.

To evaluate the control performance, the deviation results are shown in Tables 1 and 2. The smaller depth deviation and smaller yaw angle deviation can be achieved, and then both the feasibility and the superiority of the proposed LMPC controller has been preliminarily verified. In the cooperative control strategy, the DMPC controller transforms control objectives of the RDMV into individual motion control of TROV and HROV. Since the LMPC controller has been proven feasible for

ROV's individual control, the proposed LMPC controller is theoretically feasible for the RDMV.

4.2. Parameters set

The dynamic model of the RDMV deduced in Section 2 is used as the controlled object, where scale models are used. Besides, uncertain nonlinear dynamics learned by the NPL method are considered as unknown. OCPs (43) and (44) are solved by MATLAB function "quadprog (·)". OCPs (55) and (58) are solved by MATLAB function "fmincon(·)".

To verify the superiority of the proposed cooperative control strategy, a comparative numerical simulation is conducted. The only difference with the proposed cooperative control strategy is that the state transition models become:

$$\begin{aligned} \mathscr{X}_2(k+1) &= \mathscr{A}_2\mathscr{X}_2(k) + \mathscr{B}_2U_2(k) + g_2(\mathscr{X}_2(k)), \\ \mathscr{X}_3(k+1) &= \mathscr{A}_3\mathscr{X}_2(k) + \mathscr{B}_3U_3(k) + g_3(\mathscr{X}_3(k)) \end{aligned} \tag{78}$$

where the model mismatch from parametric uncertainties and external disturbance is not considered in the state transition models.

Parameters of the RDMV scaled model are shown in Table 3, where the hydrodynamic parameters of the TROV and HROV are set as the same, and parameters of the soft seafloor sediment are from [27,29,34].

Parameters in optimal control problems have great influence on control performance. In order to intuitively verify the superiority of the cooperative control strategy, weight matrices and constraints are all set as the same. Table 4 shows the parameters used in optimal control problems (43), (44), (55) and (58). For the NPL method used in the LMPC controllers, the nominal minimum number of sample points is set as: $N_{\overline{\mathscr{Z}}_1} = N_{\overline{\mathscr{Z}}_2} = 5$. The estimated Lipschitz constants are set as:$L_{n2} = 0.5578, L_{n3} = 0.7957$.

4.3. Learning performance evaluation

Note that the proposed NPL method is mainly developed from [18]. To intuitively demonstrate its superiority, numerical simulations are conducted on the stabilization control of the system from the literature [18]. As the results recorded in Table 5, the mean square error of the proposed NPL method is smaller than that of the comparative NPL method. After offline training, the number of the sample points in the proposed NPL method is nearly half of the comparative NPL method. Since the time complexity of the KI prediction equation is positively correlated with the number of samples, the simulation time for the whole stabilization control of the proposed NPL Method can be reduced by approximately 33 %.

As shown in Fig. 4 and Fig. 5, the estimated value fits the actual value well, and NPL estimated error is bounded. The absolute value of the NPL estimated error is less than the conservative upper bound in Theorem 2. From the histograms in Fig. 4 left and Fig. 5 left, NPL estimated error shows a trend of normal distribution. In more detail, estimated values $\widehat{f}_1^3$ and $\widehat{f}_1^2$ are more likely approach the noise upper bound with a sinusoidal trend. It can be seen that estimated values $\widehat{f}_2^3$, $\widehat{f}_2^2$, $\widehat{f}_3^3$ and $\widehat{f}_3^2$ also fit the actual values better, where it also shows a sinusoidal trend. The difference is that the amplitudes of $\widehat{f}_1^3$ and $\widehat{f}_1^2$ are larger. Besides, estimated values $\widehat{f}_4^3$ and $\widehat{f}_4^2$ are far much smaller than the noise upper bound, and fits the actual values best, whose amplitude is far smaller. Compared with the estimated values and the measured values with noise, it can be seen that process noise is filtered to some extent by the NPL method.

4.4. Cooperative control performance verification

To visually show the superiority of the proposed cooperative control strategy, the control trajectory of the proposed cooperative control strategy and the comparative numerical simulation are shown Fig. 6. From Fig. 6(a), the MRT's path tracking trajectory under "LMPC" fits the reference trajectory accurately, and the HROV can keep synchronization with the MRT. However, the MRT's path tracking trajectory under "MPC" fails to track the reference trajectory, especially at the amplitude of the sine curve. The MRT's average path tracking deviation is up to 0.32 m, and the MRT's max average path tracking deviation is up to 0.81 m. The HROV also fails to keep synchronization with the MRT. The HROV's average synchronization deviation is up to 0.32 m, and the MRT's max synchronization deviation is up to 0.81 m. As the MRT's body sinkage shown in Fig. 6(b), using the proposed cooperative control strategy, the HROV can successfully keep the MRT's body subsidence by applying a vertical pulling force via the two-force member. However, the MRT fails to keep its body subsidence in the comparative numerical simulation. The MRT's average sinkage deviation is up to 0.03 m, and MRT's max sinkage deviation is up to 0.08 m.

As shown in Section 4.3, the RDMV's functions expressed in Eq. (30) and Eq. (31) can be accurately estimated, and the enhanced NPL method is effective to address the model mismatch of the state transition model. In the comparative numerical simulation, there is no strategy to address the model mismatch, leading to an inaccurate state transition model. Since the difference between the control trajectory of the proposed cooperative control strategy and that of the comparative numerical simulation is the state transition model, and the enhanced NPL method that obtain an accurate state transition model in optimal control problem (55). Besides, the model-based control law can meet the control objectives of the RDMV, and the validity of the state transition model utilized in the LMPC controller can be proven, and the accurate state transition model can achieve better control performance.

Since the control performance of MPC controller depends on its parameters, parameters that are consistent with the LMPC controller may not necessarily achieve the desired control performance. The parameters of the MPC controller are reset through trial and error, and the reset parameters are listed in Table 6. The simulation results are documented in Tables 7 and 8. It can be seen that the MRT's average path tracking deviation is reduced by approximately 71 %, while the max path tracking deviation is reduced by around 68 %. The MRT's average sinkage deviation is reduced by approximately 33 %, while the max path tracking deviation is reduced by 50 %. For the HROV's synchronization deviation, the average deviation is reduced by 75 %, and the max deviation is reduced by 70 %. It can be seen that appropriate MPC parameters can enhance its robustness against the model mismatch. However, the deviation evaluation metrics for the MPC controller are still significantly larger than that for the LMPC controller. Such a comparison also visually demonstrates the superiority of the LMPC controller.

As the RDMV's state using the proposed cooperative control strategy shown in Fig. 6(c) and Fig. 6(d), the TROV can tow the MRT to keep the desired surge speed, and the HROV can also maintain the surge speed synchronization with the MRT. For the sway speed, the heave speed, the yaw rate and the horizontal rotation angle of the TROV, they show the sinusoidal variation trend with random chattering.

To analyze the robustness of the LMPC controller and further explain the trend, numerical simulation results under the different environmental disturbance cases using the proposed cooperative control strategy are shown in Fig. 7 and Table 7. From Fig. 7(a) and Fig. 7(b), the values of the path tracking deviation and the synchronization deviation under the case "NoOcdRan" is are essentially zero. Under this case, the model mismatch from parametric uncertainties is considered, and the LMPC controller can effectively handle it. Under the case "Ocd", the completely unknown complex sinusoidal disturbance is considered. Since the length and width of the MRT are 2 m and 1.4 m, respectively. the values of path tracking deviation and the synchronization deviation under the case "Ocd" are relatively small enough. It can be seen that the LMPC controller is robust against the complex sinusoidal disturbance. Under the two cases "OcdRanGs" and t "OcdRan", the bounded process noise from uniform and Gaussian distributions is additionally introduced, and the path tracking deviation and the synchronization deviation are only a litter larger than that of “Ocd”. Since the values of the two cases are almost the same, the LMPC controller could achieve good cooperative control performance suffered from the two kinds of process noise. It can be seen the LMPC controller is robust against the model mismatch consisted of the parametric uncertainties, the external disturbances under the process noise.

From Fig. 7(c) and (d), control input under the case “NoOcdRan” is relatively smooth. Since the TROV plays a role of the steer mechanism in the RDMV, which is driven by the control input T_{N2}. Range of the control input T_{N2} around “0”, which is influenced by the controller parameters, mainly dynamically adjust the horizontal rotation angle of the TROV to converge the path tracking deviation. Compared with the control input under the case “Ocd”, the control input seems add a sinusoidal trend. Note that the ocean current disturbance is mainly sinusoidal signal, and the control input correspondingly addresses the disturbance with a similar changing trend. Compared with the control input under the two cases “OcdRan” and “OcdRanGs”, it adds a random chattering trend. Similarly, the control input correspondingly addresses the external disturbance and the process noise. It can also be explained that the range in Fig. 7(c) and (d) is a sinusoidal variation trend with random chattering.

Finally, the computing time of optimal control problems (55) and (58) is recorded in Table 9 to evaluate the real-time performance of the LMPC controller. “MPC-2” and “MPC-3” denote the computing time optimal control problems (55) and (58) in the comparative numerical simulation. “LMPC-2” and “LMPC-3” denote that of the proposed cooperative control strategy. It can be seen the computing time of the “MPC” is almost the same as the that of the “LMPC”. That means the NPL method will not bring much computational burden, and good real-time performance can be ensured.

5. Conclusion

In this study, an enhanced ROV-based deep-sea mining system is proposed, and the cooperative control strategy of the RDMV is studied based on three-dimensional space model. For the dynamic model of the RDMV, the TROV and the MRT are analogized as the front and rear wheels of an Ackermann steering vehicle in the horizontal plane. The HROV’s relative position to MRT is obtained by the rotation angles of the two-force member, the dynamics of the rotation angles is analyzed based on the deduce of the angular acceleration in rigid body kinematic. For the cooperative control strategy, the DMPC controller is developed to separately construct optimal control problems to obtain the virtual law to meet the cooperative control objects. The enhanced NPL can accurately estimate the uncertain dynamics of the RDMV with good real-time performance, and LMPC controller is utilized to construct optimal control problems to track the virtual law with the estimated dynamics introduced in the state transition model.

The KI prediction equation is calculated once per prediction horizon, and good real-time performance can’t be ensured for long prediction horizon. Since long prediction horizon may achieve better control performance in some special conditions, we plan to enhance the NLP method for a LMPC controller with long prediction horizon in our future work. Since the learning performance of the enhanced NPL method and the cooperative control performance have been verified by the numerical simulation, a convincing demonstration would require experimental verification. In our future work, basic experiments in indoor environment for a scaled RDMV will be conducted.

Author declarations

The authors have no conflicts to disclose. We confirm that this manuscript is neither under consideration nor has been published in any other venue elsewhere.

Funding

This research work was funded by the National Natural Science Foundation of China (Grant No. 52071138), the Basic Research Program of Jiangsu (Grant No. BK20243019) and the Guangdong Basic and Applied Basic Research Foundation (Grant No. 2024A1515010683).

CRediT authorship contribution statement

Xu Daolin: Supervision, Resources, Project administration. **Zhang Haihua:** Validation, Resources, Project administration. **Zou Weisheng:** Supervision, Project administration, Funding acquisition, Conceptualization. **Zhang Haicheng:** Writing – review & editing, Visualization, Validation, Supervision, Project administration, Methodology, Investigation, Formal analysis, Conceptualization. **Chen Yuheng:** Writing – original draft, Visualization, Validation, Software, Methodology, Investigation, Formal analysis, Data curation, Conceptualization.

Declaration of Competing Interest

The authors declare that they have no known competing financial interests or personal relationships that could have appeared to influence the work reported in this paper.

References

[1] Sha F, Xi M, Chen X, Liu X, Niu H, Zuo Y. A recent review on multi-physics coupling between deep-sea mining equipment and marine sediment. Ocean Eng 2023;276:114229.
[2] Wu H, Liu W, Jiang M, Li C, Li J, Chen B, Wang C, Chen Y. Numerical simulation investigation on parameter optimization of deep-sea mining vehicles. Chin J Mech Eng 2023;36(1):54.
[3] Gao Y, Liu L, Fu S, Chai S, Shi C. Nonlinear dynamics of a vertical pipe subjected to a two-phase, solid-liquid internal flow. Appl Math Model 2023;120:651–66.
[4] Wang L, Chen X, Wang L, Li Z, Yang W. Mechanical properties and soil failure process of interface between grouser of tracked mining vehicle and deep-sea sediment. Ocean Eng 2023;285:115336.
[5] Zou W., Zhang H., Chen Y. An introduction to rov based intelligent deep sea mining system. presented at the the 20th international conference on transport and sedimentation of solid particles. Wroclaw, Poland; 2023.
[6] Chen Y, Zhang H, Zou W, Zhang H, Zhou B, Xu D. Dynamic modeling and learning based path tracking control for ROV-based deep-sea mining vehicle. Expert Syst Appl 2025;262:125612.
[7] Zeng Z, Yue W, Zhu L. Finite-time fuzzy cooperative control for multi-AUV systems under cyber-attacks with hybrid unknown nonlinearities. Ocean Eng 2024;304:117875.
[8] Jia Z, Lu H, Chen H, Zhang W. Robust distributed cooperative rendezvous control for heterogeneous marine vehicles using model predictive control. IEEE Trans Veh Technol 2024;73(8):11002–13.
[9] Bian Y, Zhang J, Hu M, Du C, Cui Q, Ding R. Self-triggered distributed model predictive control for cooperative diving of multi-AUV system. Ocean Eng 2023;267:113262.
[10] Aryan P, Raja GL, Vilanova R, Meneses M. Repositioned internal model control strategy on time-delayed industrial processes with inverse behavior using equilibrium optimizer. IEEE Access 2023;11:54556–68.
[11] Mayne DQ. Model predictive control: recent developments and future promise. Autom, Artic 2014;50(12):2967–86.
[12] Yang Z, Li S, Yang S. Anti-roll trajectory tracking control based on adaptive weight allocation law in phase space stable region. IEEE Trans Veh Technol 2024;73(12):18208–21.
[13] Chen Y, Zhang H, Zhou X, Guo B, Xu D. Hybrid control strategy for efficiency enhancement of a raft-type wave energy converter. Energy 2024;300:131519.
[14] Tran C, Øveraas H, Johansen TA. ROV recovery with wave-motion compensation using model predictive control. Ocean Eng 2024;293:116764.
[15] Luo G, Gao S, Jiang Z, Luo C, Zhang W, Wang H. ROV trajectory tracking control based on disturbance observer and combinatorial reaching law of sliding mode. 2024/07/15/ Ocean Eng 2024;304:117744.
[16] Long C, Hu M, Qin X, Bian Y. Hierarchical trajectory tracking control for ROVs subject to disturbances and parametric uncertainties. Ocean Eng 2022;266:112733.
[17] Mitsioni I, Tajvar P, Kragic D, Tumova J, Pek C. Safe data-driven model predictive control of systems with complex dynamics. IEEE Trans Robot 2023;39(4):3242–58.
[18] Zheng K, Shi D, Shi Y, Wang J. Nonparametric event-triggered learning with applications to adaptive model predictive control. IEEE Trans Autom Control 2023;68(6):3469–84.
[19] Zhang X, Liu J, Xu X, Yu S, Chen H. Robust learning-based predictive control for discrete-time nonlinear systems with unknown dynamics and State Constraints. IEEE Trans Syst Man Cyber: Syst 2022;52(12):7314–27.

[20] Park J, Jeon S, Han S. Model-based reinforcement learning with probabilistic ensemble terminal critics for data-efficient control applications. IEEE Trans Ind Electron 2024;71(8):9470–9.
[21] Wang M, Lou X, Wu W, Cui B. Koopman-based MPC with learned dynamics: hierarchical neural network approach. IEEE Trans Neural Netw Learn Syst 2024;35(3):3630–9.
[22] Zabinsky ZB, Smith RL, Kristinsdottir BP. Optimal estimation of univariate black-box Lipschitz functions with upper and lower error bounds. Comput Oper Res 2003;30(10):1539–53.
[23] Kandel A, Moura SJ. Safe learning MPC with limited model knowledge and data. IEEE Trans Control Syst Technol 2024;32(2):472–87.
[24] Calliess J-P, Roberts SJ, Rasmussen CE, Maciejowski J. Lazily adapted constant kinky inference for nonparametric regression and model-reference adaptive control. Automatica 2020;122:109216.
[25] Xu Z, et al. Research on contact model of track-soft sediment and traction performance of four-tracked seabed mining vehicle. Ocean Eng 2022;259:111902.
[26] Sun C, Li Q, Li B, Li L. A successive linearization in feasible set algorithm for vehicle motion planning in unstructured and low-speed scenarios. IEEE Trans Intell Transp Syst 2022;23(4):3724–36.
[27] Dai Y, Xue C, Su Q, Huang X. Numerical analysis on hydrodynamic characteristics of a deep-sea mining vehicle under three typical motions. Ocean Eng 2021;235:109446.
[28] Chen Q, Yang J, Mao J, Liang Z, Lu C, Sun P. A path following controller for deep-sea mining vehicles considering slip control and random resistance based on improved deep deterministic policy gradient. Ocean Eng 2023;278:114069.
[29] Al-Milli S, Seneviratne LD, Althoefer K. Track–terrain modelling and traversability prediction for tracked vehicles on soft terrain. J Terra 2010;47(3):151–60.
[30] Ruslan NAI, Amer NH, Hudha K, Kadir ZA, Ishak SAFM, Dardin SMFS. Modelling and control strategies in path tracking control for autonomous tracked vehicles: a review of state of the art and challenges. J Terra 2023;105:67–79.
[31] Yamada M, Yamauchi G, Hashimoto T. Fundamental study on underwater trafficability for tracked vehicle. J Terra 2021;98:42–9.
[32] Kar MK. Prediction of track forces in skid-steering of military tracked vehicles. J Terra 1987;24(1):75–84.
[33] Liu CH, Wong JY. Numerical simulations of tire-soil interaction based on critical state soil mechanics. J Terra 1996;33(5):209–21.
[34] Zeng R, Kang Y, Yang J, Qin B, Chen S, Cao D. An integrated terrain identification framework for mobile robots: system development, analysis, and verification. IEEE/ASME Trans Mechatron 2021;26(3):1581–90.
[35] Yu S, Maier C, Chen H, Allgöwer F. Tube MPC scheme based on robust control invariant set with application to Lipschitz nonlinear systems. Syst Control Lett 2013;62(2):194–200.
[36] Chen Y, Bian Y. Tube-based event-triggered path tracking for AUV against disturbances and parametric uncertainties. Electron Artic 2023;12(20):4248.
[37] Chen Y, Bian Y, Cui Q, Dong L, Xu B, Hu M. LTVMPC for Dynamic Positioning of An Autonomous Underwater Vehicle. In: 2021 5th CAA International Conference on Vehicular Control and Intelligence. CVCI; 2021.
[38] Tijjani AS, Chemori A, Creuze V. Robust adaptive tracking control of underwater vehicles: design, stability analysis, and experiments. IEEE/ASME Trans Mechatron 2021;26(2):897–907.